Abrupt excursions in water vapor isotopic variability at the Pointe Benedicte observatory on Amsterdam Island

Amaëlle Landais[1,*], Cécile Agosta[1,*], Françoise Vimeux[1,2], Olivier Magand[3], Cyrielle Solis[1], Alexandre Cauquoin[4], Niels Dutrievoz[1], Camille Risi[5], Christophe Leroy-Dos Santos[1], Elise Fourré[1], Olivier Cattani[1], Olivier Jossoud[1], Bénédicte Minster[1], Frédéric Prié[1], Mathieu Casado[1], Aurélien Dommergue[6], Yann Bertrand[6], Martin Werner[7]

[1] Laboratoire des Sciences du Climat et de l'Environnement, LSCE/IPSL, CEA-CNRS-UVSQ, Université Paris-Saclay, 91191 Gif-sur-Yvette, France

[2] HydroSciences Montpellier (HSM), UMR 5569 (UM, CNRS, IRD), 34095 Montpellier, France

[3] Observatoire des Sciences de l'Univers à La Réunion (OSU-R), UAR 3365, CNRS, Université de La Réunion, Météo France, IRD, 97744 Saint-Denis, La Réunion, France

[4] Institute of Industrial Science (IIS), The University of Tokyo, Kashiwa, Japan.

[5] Laboratoire de Météorologie Dynamique, Institut Pierre - Simon Laplace, Sorbonne Université / CNRS / École Polytechnique – IPP, Paris, France

[6] Univ. Grenoble Alpes, CNRS, INRAE, IRD, Grenoble INP[T], IGE, 38000 Grenoble, France ([T]Institute of Engineering and Management Univ. Grenoble Alpes)

[7] Alfred Wegener Institute, Helmholtz Centre for Marine and Polar Research, D-27570 Bremerhaven, Germany

* corresponding authors who contributed equally to the study: amaelle.landais@lsce.ipsl.fr and cecile.agosta@lsce.ipsl.fr

31 **Abstract**

32 In order to complement the picture of the atmospheric water cycle in the Southern Ocean, we

33 have continuously monitored water vapor isotopes since January 2020 on Amsterdam Island in

34 the Indian Ocean. We present here the first 2-year-long water vapor isotopic record on this site.

35 We show that the water vapor isotopic composition largely follows the water vapor mixing

36 ratio, as expected in marine boundary layers. However, we detect 11 periods of a few days

37 where there is a strong loss of correlation between water vapor $\delta^{18}O$ and water vapor mixing

38 ratio as well as abrupt negative excursions of water vapor $\delta^{18}O$. These excursions often occur

39 toward the end of precipitation events. Six of these events show a decrease in gaseous elemental

40 mercury suggesting subsidence of air from higher altitude.

41 Our study aims at further exploring the mechanism driving these negative excursions in water

42 vapor $\delta^{18}O$. We used two different models to provide a data-model comparison over this 2-year

43 period. While the European Centre Hamburg model (ECHAM6-wiso) at 0.9° was able to

44 reproduce most of the sharp negative water vapor $\delta^{18}O$ excursions hence validating the physics

45 process and isotopic implementation in this model, the Laboratoire de Météorologie

46 Dynamique Zoom model (LMDZ-iso) at 2° (3°) resolution was only able to reproduce 7 (1) of

47 the negative excursions highlighting the possible influence of the model resolution for the study

48 of such abrupt isotopic events. Based on our detailed model-data comparison, we conclude that

49 the most plausible explanations for such isotopic excursions are rain-vapor interactions

50 associated with subsidence at the rear of a precipitation event.

51

1. Introduction

The main sources of uncertainty in the atmospheric components of Earth System Models for future climate projections are associated with complex atmospheric processes, particularly those related to water vapor and clouds (Arias et al., 2021; Sherwood et al., 2014). Decreasing these uncertainties is of vital interest as the hydrological cycle is a fundamental element of the climate system because it allows, via the transport of water vapor, to ensure the Earth's thermal balance.

Stable water isotopes are a useful tool to study the influence of dynamical processes on the water budget at various spatial and temporal scales. They provide a framework for analyzing moist processes over a range of time scales from large-scale moisture transport to cloud formation, precipitation, and small-scale turbulent mixing (Bailey et al., 2023; Dahinden et al., 2021; Galewsky et al., 2016; Thurnherr et al., 2020).

The relative abundance of heavy and light isotopes in different water reservoirs is altered during phase change processes due to isotopic fractionation (caused by a difference in saturation vapor pressure and molecular diffusivity in the air and the ice). Each time a phase change occurs, the relative abundance of water vapor isotopes is altered. We express the abundance of the heavy isotopes D and ^{18}O with respect to the amount of light isotopes H and ^{16}O, respectively, in the water molecules through the notation δ:

$$\delta^{18}O = \left(\frac{\left({^{18}O}/{_{16}O} \right)_{Sample}}{\left({^{18}O}/{_{16}O} \right)_{VSMOW}} - 1 \right) \times 1000 \quad \text{(Eq. 1)}$$

$$\delta D = \left(\frac{\left({D}/{H} \right)_{Sample}}{\left({D}/{H} \right)_{VSMOW}} - 1 \right) \times 1000 \quad \text{(Eq. 2)}$$

where (^{18}O/^{16}O) and (D/H) represent the isotopic ratios of oxygen and hydrogen atoms in water and VSMOW (Vienna Standard Mean Ocean Water) is an international reference standard for water isotopes.

There are two types of isotopic fractionation: equilibrium fractionation, which is caused by the difference in saturation vapor pressure of different isotopes, and non-equilibrium fractionation, which occurs due to molecular diffusion (e.g. during ocean evaporation in undersaturated atmosphere or snowflakes condensation in oversaturated atmosphere). In the water vapor above the ocean, the proportion of non-equilibrium fractionation, and hence diffusive processes can

81 be estimated by the deuterium excess, a second order isotopic variable denoted d-excess,
82 defined as (Dansgaard, 1964):

83

84   d-excess=$\delta D - 8 \times \delta^{18}O$ (Eq.3)

85

86 Over the recent years and thanks to the development of optical spectroscopy enabling
87 continuous measurements of water isotopes ratios in water vapor, an increasing number of
88 studies have focused on the use of water vapor stable isotopes to document the dynamics of the
89 water cycle over synoptic weather events, such as cyclones, cold fronts, atmospheric rivers
90 (Aemisegger et al., 2015; Ansari et al., 2020; Bhattacharya et al., 2022; Dütsch et al., 2016;
91 Graf et al., 2019; Lee et al., 2019; Munksgaard et al., 2015; Tremoy et al., 2014) or water cycle
92 processes such as evaporation over the ocean or deep convection (Benetti et al., 2015; Bonne
93 et al., 2019). Several instruments have been installed either in observatory stations (e.g.
94 Aemisegger et al., 2012; Guilpart et al., 2017; Leroy-Dos Santos et al., 2020; Steen-Larsen et
95 al., 2013; Tremoy et al., 2012), on boat (e.g. Benetti et al., 2014; Thurnherr et al., 2019) or on
96 aircraft (Henze et al., 2022). In the aforementioned studies, the interpretation of the isotopic
97 records is often performed using a hierarchy of isotopic models, from conceptual models
98 (Rayleigh type) to general circulation models or regional weather prediction models equipped
99 with water isotopes (Ciais and Jouzel, 1994; Markle and Steig, 2022; Risi et al., 2010; Werner
100 et al., 2011). Such data comparisons enable one to test the performances of the models either in
101 the simulation of the dynamic of the atmospheric water cycle or in the implementation of the
102 water isotopes. Our study is part of these dynamics analyses and aims at improving the
103 documentation of climate and atmospheric water cycle in the Southern Indian Ocean, a region
104 which has been poorly documented until now.
105 Over the previous years, we have installed three water vapor analyzers on La Reunion Island at
106 the Maïdo observatory, 21.079°S, 55.383°E, 2160m (Guilpart et al., 2017) and in Antarctica
107 (Dumont d'Urville, 66,663°S, 140°E, 202m and Concordia, 75.1°S, 123.333°E, 3233m; Bréant
108 et al., 2019; Casado et al., 2016; Leroy-Dos Santos et al., 2021). These instruments have been
109 used for the following purposes. They document the diurnal variability of the isotopic signal
110 with the influence of the subtropical westerly jet on the water isotopic signal in night as well as
111 the cyclonic activity on La Réunion Island. In Antarctica, the records have shown a strong
112 influence of katabatic winds on the isotopic composition of water vapor (Bréant et al., 2019).
113 In order to complete the picture of the atmospheric water cycle over the Indian basin of the
114 Southern Ocean already measured by these three analyzers, we installed a new water vapor

isotopic analyzer in the mid-latitude of the south Indian Ocean on Amsterdam Island (Figure 1) in November 2019. Amsterdam Island is one of the very rare atmospheric observatories in the southern hemisphere. Moreover, the south Indian Ocean is a significant moisture source for Antarctic precipitation, notably in the region encompassing Dumont d'Urville and Concordia stations (Jullien et al., 2020; Wang et al., 2020).

The objective of this study is to provide the first analyses of isotopic records (vapor and precipitation) on Amsterdam Island, with a comparison of meteorological data and environmental data collected in parallel on the Amsterdam Island Observatory (e.g. atmospheric mercury) to help with the interpretation of isotopic records. This study includes analyses of meteorological maps, back trajectories as well as outputs from general circulation models equipped with water isotopes. After a description of the different records over the years 2020 and 2021, model simulations and back trajectories, we focus on some low-pressure events associated with a strong negative excursion of $\delta^{18}O_v$ over a few days and a decoupling between $\delta^{18}O_v$ and humidity. These events are then used for evaluation of to evaluate atmospheric component of Earth system models equipped with water isotopes.

2. Methods

2.1 Site

Labelled as a global site for the Global Atmosphere Watch World Meteorological Organization, Amsterdam Island (37.7983° S, 77.5378° E) is a remote and very small island of 55 km^2 with a population of about 30 residents, located in the southern Indian Ocean at 3300 km and 4200 km downwind from the nearest lands, Madagascar, and South Africa, respectively (Sprovieri et al., 2016). Climate is temperate, generally mild with frequent presence of clouds (average total sunshine hours is 1581 hours per year over the period 1981 – 2010 from MeteoFrance data). Seasonal boundaries are defined as follows: winter from July to September and summer from December to February, in line with previous studies (Sciare et al., 2009). Average temperature is lower in winter compared to summer (10.5°C vs 15°C) while relative humidity and wind speed remain high (50-85% and 5 to 15 m s^{-1} respectively) most of the year without a clear seasonal cycle.

Numerous atmospheric compounds and meteorological parameters are and were continuously monitored at the site since 1960 (Angot et al., 2014; El Yazidi et al., 2018; Gaudry et al., 1983; Gros et al., 1999, 1998; Polian et al., 1986; Sciare et al., 2000, 2009; Slemr et al., 2015; Slemr et al., 2020). In particular, the Amsterdam (AMS) site hosts several dedicated atmospheric

148 observation instruments notably at the Pointe Bénédicte atmospheric observatory (70 m above

149 sea level) where greenhouse gases concentrations and mercury (Hg) are monitored. Hg species

150 have been continuously measured since 2012.

151
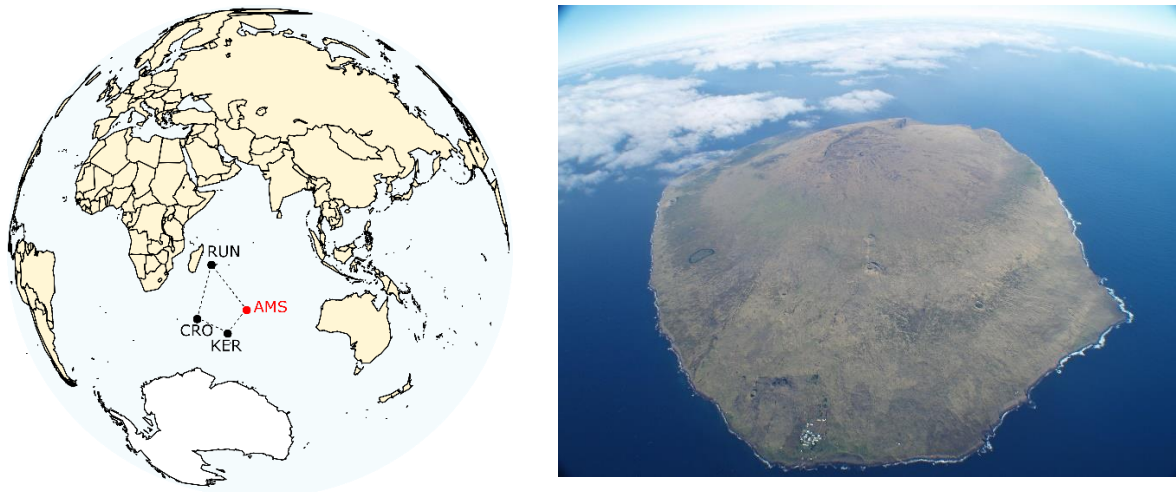
152

153 **Figure 1** : Location (left) and picture (right) of Amsterdam Island. CRO: Crozet Island;

154 RUN: La Réunion Island; KER: Kerguelen Island; AMS: Amsterdam Island.

155 Picture credit: left – Magand adapted from (Angot et al., 2016); right – photo taken by

156 O. Magand.

157

158 **2.2 Long term measurements**

159 2.2.1 Meteorological measurements

160

161 One meteorological station is installed at the top of an observation mast (25 m above ground

162 level, hence 95 m above sea level) at the Pointe Bénédicte observatory since 1980 (data used

163 during this study). Wind speed and direction, atmospheric pressure, air temperature and relative

164 humidity data are currently obtained at a minute resolution. Another meteorological station is

165 based on the island and is operated by Météo France at Martin-de-Viviès life base around 27 m

166 above sea level, about two kilometers east from the Pointe Bénédicte observatory collecting air

167 temperature, humidity, precipitation, wind speed and direction, pressure and solar radiation

168

169 2.2.2 Gaseous elemental mercury (GEM)

170

Atmospheric GEM (Gaseous Elemental Mercury) measurements have been conducted since 2012 in the framework of IPEV GMOStral-1028 observatory program at the Pointe Benedicte atmospheric research facility (Magand and Dommergue, 2022). GEM is continuously measured (15-minute data frequency acquisition) using a Tekran 2537 A/B instrument model (Angot et al., 2014; Li et al., 2023; Slemr et al., 2015, 2020; Sprovieri et al., 2016). The measurement is based on mercury enrichment on a gold cartridge, followed by thermal desorption and detection by cold vapor atomic fluorescence spectroscopy (Bloom and Fitzgerald, 1988; Fitzgerald and Gill, 1979). Concentrations are expressed in nanograms per cubic meters at standard temperature and pressure conditions (273.15 K and 1013.25 hPa) with an instrumental detection limit below 0.1 ng m^{-3} and a GEM average uncertainty value around 10% (Slemr et al., 2015). The instrument is automatically calibrated following a strict procedure adapted from that of Dumarey et al. (1985). Ambient air is sampled at 1.2 L min^{-1} through a heated (50°C) and UV protected PTFE sampling line, with an inlet installed outside, 6 m above ground level (76 m above sea level). The air is filtered through two 0.45 µm pore size polyether sulphone and one PTFE (polytetrafluoroethylene) 47 mm diameter filters before entering in Tekran to prevent the introduction of any particulate material into the detection system as well as to capture any gaseous oxidized mercury or particulate bound mercury species ensuring that only GEM is sampled. To ensure the comparability of mercury measurements around the world, the instrument is operated according to the Global Mercury Observation System standard operating procedures (Sprovieri et al., 2016; Steffen et al., 2012).

In this study, and even if long-range transport and a variable tropopause height may modulate the signal, atmospheric GEM is used as potential tracer of stratosphere-to-troposphere intrusion and/or subsidence of upper troposphere (above 5-6 km) that may impact the atmospheric records at the Pointe Benedicte Observatory where marine boundary layer is collected most of the time (Angot et al., 2014; Slmer et al., 2015, 2020; Sprovieri et al., 2016). Mercury in the atmosphere consists of three forms: gaseous elemental mercury (GEM as defined above), gaseous oxidized mercury and particulate-bound mercury. GEM, the dominant form of atmospheric mercury, is ubiquitous in the atmospheric reservoir and originates from a multitude of anthropogenic and natural sources (Edwards et al., 2021; Gaffney et al., 2014; Gustin et al., 2020 ; Gworek et al., 2020). Near the surface (marine or terrestrial boundary layer) and out of polar regions, gaseous oxidized mercury and particulate-bound mercury represent only a few percent of the total atmospheric mercury (Gustin and Jaffe, 2010; Gustin et al., 2015; Swartzendruber et al., 2006). Chemical cycling and spatiotemporal distribution of mercury in the air is still poorly understood whatever atmospheric layer considered (surface, mixed or free

troposphere, stratosphere), and complete GEM oxidation schemes remain unclear (Shah et al., 2021 and associated references). Still, several studies provided evidence that vertical distribution of atmospheric mercury measurements from boundary layer to lower/upper troposphere and stratosphere shows a decreasing trend in GEM concentration with increasing altitude, in parallel with an increase in the concentration of divalent mercury resulting from GEM oxidation mechanisms (Brooks et al., 2014; Fain et al., 2009; Fu et al., 2016; Koenig et al., 2023; Lyman and Jaffe, 2012; Murphy et al., 2006; Swartzendruber et al., 2006, 2008; Sheu et al., 2010; Talbot et al., 2007). The identification of such observational processes (lower GEM concentrations in high-altitude air masses versus marine boundary layer ones) is used here to help characterizing possible high altitude air masses intrusions at low altitude Pointe Benedicte Observatory.

2.3 Water vapor isotopic measurements

The near-surface water vapor $\delta^{18}O$ and δD (hereafter $\delta^{18}O_v$ and δD_v expressed in ‰ versus SMOW and enabling to calculate water vapor d-excess$_v$ as d-excess$_v = \delta D_v - 8 \times \delta^{18}O_v$) and the water vapor mixing ratio (q_v in ppmv) have been measured continuously since November 2019. The measurements have been done with a Picarro Inc. instrument (L2130-i model) based on wavelength-scanned cavity ring down spectroscopy. The instrument has been installed in a temperature-controlled room at the Amsterdam Island observatory and the sampling of water vapor is done outside at ~ 6 m above ground level (or 76 m above sea level) through a 5 m long inlet tube made of PFA (perfluoroalkoxy alkanes) and heated at 40°C.
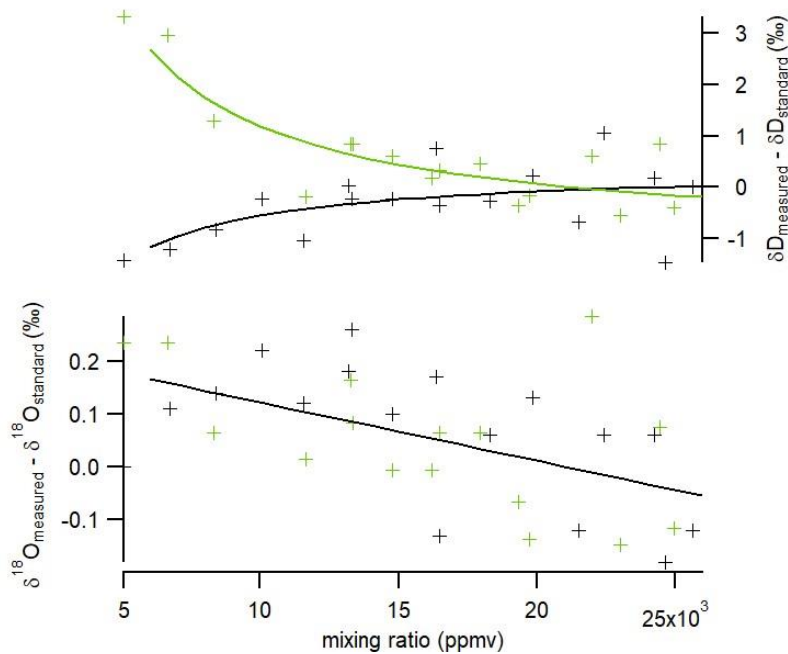
Figure 2: Influence of the water vapor mixing ratio on measured δD (top) and δ¹⁸O (bottom) (anomaly from the true value of the standard). The results are shown for two different standards (GREEN_AMS in green and EPB_AMS in black). The crosses indicate the data obtained with the set-up and the solid lines are the best regression curves (same curve for $\delta^{18}O$ for both standards).

The calibration of water vapour mixing ratio was performed in the laboratory before sending the instrument. In the field, we found an excellent agreement between mixing ratio measured by the Picarro instrument and mixing ratio measured by the weather station (the difference between the two records always stays below 2% and there is no systematic shift between the two records).

The calibration of the water isotopic data is performed in several steps following previous studies (Leroy-Dos Santos et al., 2020; Tremoy et al., 2011) and using a standard delivery module by Picarro. First, we quantified the influence of the water vapor mixing ratio on the water isotope ratios. This effect is large at very low humidity (Leroy-Dos Santos et al., 2021). It can also depend on the isotopic composition of the standard water (Weng et al., 2020). Here, we introduced two different water standards, EPB-AMS and GREEN-AMS, with respective values of (-5.66 ‰, -47.31 ‰) and (-32.65 ‰, -263.76 ‰) for the couple ($\delta^{18}O$, δD) which encompass the isotopic values observed on site. While we would expect a constant null value for ($\delta^{18}O_{measured}$- $\delta^{18}O_{standard}$) in Figure 2 because we always inject the same water standards, the measured $\delta^{18}O$ values of both EPB-AMS and GREEN-AMS standards in fact

250 decrease with increasing humidity with the same amplitude. The ($\delta D_{measured}$-$\delta D_{standard}$)

251 displayed in Figure 2 also shows variations but in contrast to the relative evolution of $\delta^{18}O$

252 with respect to water vapor mixing ratio, the δD measurements of EPB-AMS and GREEN-

253 AMS standards exhibit different behavior: δD of EPB-AMS increases by 1.5‰ and δD of

254 GREEN-AMS decreases by 2.5 ‰ over the same 6,000-24,000 ppmv range for water vapor

255 mixing ratio q_v.

256 As a consequence, the raw $\delta^{18}O_v$ measurements are corrected with the following regression:

257

258 $$\delta^{18}O_{v,corr} = \delta^{18}O_{v,measured} + 1.1.10^{-5} \times q + 0.232 \qquad \text{(Eq 4)}$$

259

260 For the correction of the raw δD_v, we use two different regression splines for EPB-AMS and

261 GREEN-AMS (cf Figure 2):

262

263 $$\delta D_{EPB-AMS,corr} = \delta D_{EPB-AMS,measured} + \frac{9300}{q} - 0.383 \qquad \text{(Eq 5)}$$

264 $$\delta D_{GREEN-AMS,corr} = \delta D_{GREEN-AMS,measured} - \frac{22400}{q} + 1.05 \qquad \text{(Eq 6)}$$

265

266 The raw δD_v are thus weighted-corrected according to their distance to the EPB_AMS and the

267 GREEN_AMS splines as follows:

268

269

270 $$\delta D_{v,corr} = \delta D_{GREEN-AMS,corr} + \frac{\delta D_{v,measured} - \delta D_{GREEN-AMS,measured}}{\delta D_{EPB-AMS,measured} - \delta D_{GREEN-AMS,measured}} \times (\delta D_{EPB-AMS,corr} - \delta D_{GREEN-AMS,corr})$$

271 $$\text{(Eq 7)}$$

272

273 This first calibration step (correction from the influence of mixing ratio on the isotopic

274 composition) has been performed every year over the whole range of mixing ratio values and

275 provided very similar results from one year to the other.The second calibration step consists in

276 the injection of the same two isotopic standards every 47 h at a water vapor mixing ratio of

277 13,000 ppmv to correct for any long-term drift. The correction associated with this drift is less

278 than 0.4 ‰ for $\delta^{18}O$ and 2.5 ‰ for δD over the two years of measurements.

279 Precipitation were also sampled on a weekly basis in a rain gauge filled with paraffin oil which
280 permits to have measurements of water isotopic composition in the precipitation on a weekly
281 basis. The water samples are then sent for analyses to LSCE (Laboratoire des Sciences du
282 Climat et de l'Environnement) and measured with an isotopic analyzer L2130-i by Picarro. The
283 uncertainty associated with this series of measurements is of ±0.15 ‰ for $\delta^{18}O$ and ±0.7 ‰ for
284 δD leading to an uncertainty of ±1.4 ‰ for d-excess.

285

286 **2.4 Back trajectories: FLEXPART**

287
288 The origin and trajectory of air masses were calculated by FLEXPART, which is a Lagrangian
289 particle dispersion model (Pisso et al., 2019). All the meteorological data used to simulate the
290 back trajectories are taken from the ERA5 atmospheric reanalysis (Hersbach et al., 2020) with
291 a 6-hourly resolution. The ERA5 reanalysis is carried out by the European Center for Medium-
292 Range Weather Forecasts (ECMWF), using ECMWF's Earth System model IFS (Integrated
293 Forecasting System), cycle 41r2. For a few selected events, we used FLEXPART to calculate
294 back trajectories over 5 days with 1000 launches of neutral particles (sensitivity test) of inert
295 air tracers released randomly (volume of 0.1°×0.1°×100 m) every 3 hours at 100 m above sea
296 level (Leroy-Dos Santos et al., 2020) centered around the coordinates of Amsterdam Island.
297 The results of the FLEXPART back trajectories are then displayed as particle density
298 probability as well as through the location of their humidity weighted averages.

299 **2.5 General atmospheric circulation model equipped with water stable**
300 **isotopes**

301

302 **2.5.1 LMDZ-iso model (Laboratoire de Météorologie Dynamique Zoom model**
303 **equipped with water isotopes)**

304
305 LMDZ-iso (Risi et al., 2010) is the isotopic version of the atmospheric general circulation
306 model LMDZ6 (Hourdin et al., 2020). We have used LMDZ-iso version 20230111.trunk with
307 the physical package NPv6.1, identical to the atmospheric setup of IPSL-CM6A (Boucher et
308 al., 2020) used for phase 6 of the Coupled Model Intercomparison Project (CMIP6, Eyring et
309 al., 2016). We performed two simulations, one at very low horizontal resolution (VLR, 3.75°
310 in longitude and 1.9° in latitude, 96×95 grid cells) and the second at low horizontal resolution
311 (LR, 2.0° in longitude and 1.67° in latitude, 144×142 grid cells). Both simulations have 79

vertical levels and the first atmospheric level is located around 10 m above ground level. The LMDZ-iso 3D-fields of temperature and wind are nudged toward the 6-hourly ERA5 reanalysis data with a relaxation time of 3 hours. Surface ocean surface boundary conditions are taken from the monthly mean SST and sea-ice fields from the CMIP6 AMIP Sea Surface Temperature and Sea Ice dataset version 1.1.8 (Durack et al., 2022; Taylor et al., 2000). LMDZ-iso outputs are used at a 3-hourly resolution. Amsterdam Island (58 km^2) is too small to be represented in the LMDZ-iso model.

2.5.2 ECHAM6-wiso model (European Centre Hamburg model equipped with water isotopes)

ECHAM6-wiso (Cauquoin et al., 2019; Cauquoin and Werner, 2021) is the isotopic version of the atmospheric general circulation model ECHAM6 (Stevens et al., 2013). The implementation of the water isotopes in ECHAM6 has been described in detail by Cauquoin et al. (2019), and has been updated in several aspects by Cauquoin and Werner (2021) to make the model results more consistent with the last findings based on water isotope observations (isotopic composition of snow on sea ice considered, supersaturation equation slightly updated, and kinetic fractionation factors for oceanic evaporation assumed as independent of wind speed). We have used ECHAM6-wiso model outputs from a simulation with a T127L95 spatial resolution (0.9° horizontal resolution and 95 vertical levels). ECHAM6-wiso is thus run with a finer resolution than both LMDZ-iso simulations. The ECHAM6-wiso 3D-fields of temperature, vorticity and divergence as well as the surface pressure field were nudged toward the ERA5 reanalysis data (Hersbach et al., 2020) every 6 hours. The orbital parameters and greenhouse gas concentrations have been set to the values of the corresponding model year. The monthly mean sea surface temperature and sea-ice fields from the ERA5 reanalysis have been applied as ocean surface boundary conditions, as well as a mean δ^{18}O of surface seawater reconstruction from the global gridded data set of LeGrande and Schmidt (2006). As no equivalent data set of the δD composition of seawater exists, the δD of the seawater in any grid cell has been set equal to the related δ^{18}O composition, multiplied by a factor of 8, in accordance with the observed relation for meteoric water on a global scale (Craig, 1961). The ECHAM6-wiso simulation is described in detail and evaluated by Cauquoin and Werner (2021). ECHAM6-wiso outputs are given at a 6-hourly resolution. As for the LMDZ-iso model, Amsterdam Island (58 km^2) is too small to be represented by ECHAM6-wiso.

3. Results

3.1 Data description
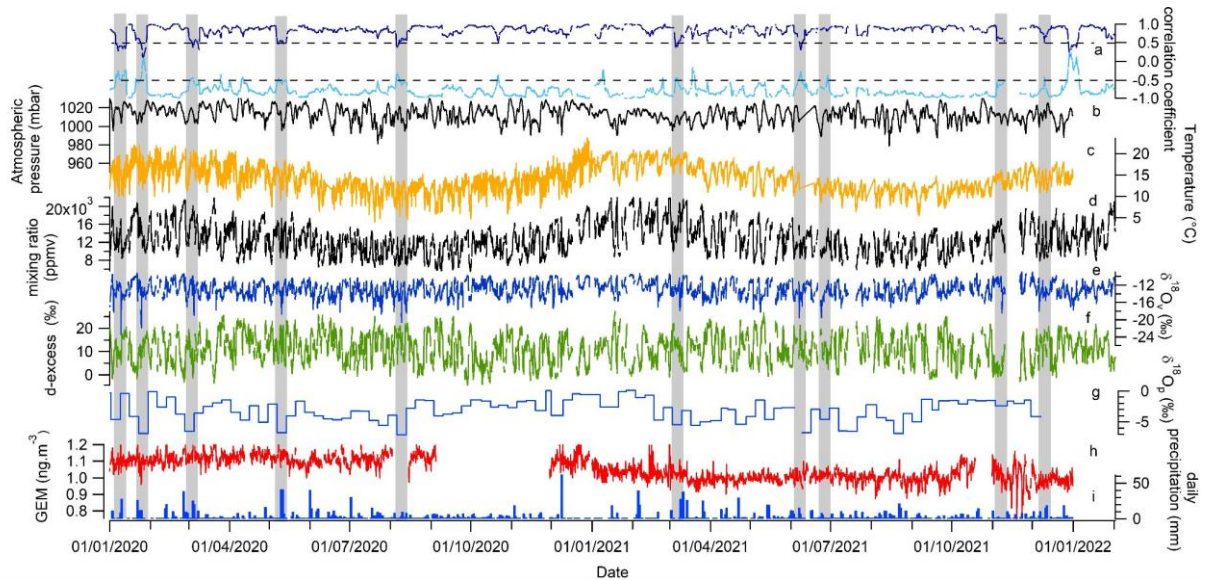
Figure 3 : Meteorological, isotopic and GEM records for the years 2020 and 2021 on the Amsterdam Island : (a) correlation coefficient between $\delta^{18}O_v$ and mixing ratio (dark blue, top) and between $\delta^{18}O_v$ and d-excess$_v$ (light blue, bottom) over a moving time window of 8 days, (b) atmospheric pressure (hourly average), (c) atmospheric temperature (hourly average), (d) water vapor mixing ratio (hourly average), (e) $\delta^{18}O_v$ (hourly average), (f) d-excess$_v$ (hourly average), (g) $\delta^{18}O$ of precipitation sampled on a weekly basis, (h) GEM concentration (hourly average), (i) daily precipitation. The grey shaded areas indicate the the negative excursions in $\delta^{18}O_v$ associated with decorrelation between water vapor mixing ratio and $\delta^{18}O_v$ and a correlation coefficient >-0.5 between d-excess$_v$ and $\delta^{18}O_v$.

3.1.1 Temporal variability in the meteorological records

As mentioned earlier, there is a clear annual cycle at Amsterdam Island as recorded in the temperature and water vapor mixing ratio for the years 2020 and 2021. The December-February period (austral summer) has the highest temperatures with an average of 15.0°C, while in winter (July-September) the average temperature varies around 10.5°C. In parallel, we do not see clear patterns of a diurnal cycle in the temperature record except for some periods yet with a small amplitude (4-5 °C).

The impact of synoptic events at the scale of a few days is visible in the temperature and water mixing ratio with a covariation of temperature and water vapor mixing ratio and amplitudes of up to 10°C and more than 10,000 ppmv.

3.1.2 Temporal variability in the GEM record

Previous studies clearly showed that AMS is little influenced by anthropogenic sources of mercury, and greatly influenced by the ocean surrounding the island (Angot et al., 2014; Hoang et al., 2023; Jiskra et al., 2018; Li et al., 2023; Slemr et al., 2015, 2020). Angot et al., 2014 reported mean annual GEM concentrations of about 1.03 ± 0.08 ng m^{-3} from 2012 to 2013. These concentrations are ~30% lower than those measured at remote sites of the northern hemisphere. Over the period 2012 to 2017, Slmer et al. (2020) confirmed that higher GEM concentrations can be found during austral winter. Lower GEM values are generally observed in October and November, as well as in January and February during austral summer. Using this 6-year long data set, mean annual GEM concentration is 1.04 ± 0.07 ng m^{-3} (annual range: 1.014 to 1.080 ng m^{-3}) i.e. very close to the one observed by Angot et al. (2014).

Surprisingly, unlike the 2012-2017 data set, GEM presented in this study did not show a significant higher mean concentration during the austral winter months than during the summer months (Figure 3), with consequently no discernible seasonal amplitude of GEM. On a finer timescale, the lack of a clear pattern of GEM seasonal cycle is counterbalanced by days showing abrupt increases or decreases in concentrations. Some of the sudden GEM decreases appear concomitant with important negative peaks of several ‰ in $\delta^{18}O_v$.

3.1.3 Temporal variability of water isotopic composition

The isotopic composition of precipitation ($\delta^{18}O_p$) sampled on a weekly basis displays a quite large variability ($\delta^{18}O_p = -3.06 \pm 1.75$ ‰, n=104) with values slightly higher during austral summer (difference between summer and winter $\delta^{18}O_p$ values is about 2 to 3 ‰) (Figure 3). No

391   significant seasonal variations are observed in the record of d-excess of precipitation (not

392   shown).

393   No diurnal cycle can be detected in the $\delta^{18}O_v$ and d-excess$_v$. An annual cycle is not visible either

394   (1 ‰ difference between summer and winter mean $\delta^{18}O_v$ value while standard deviation of the

395   entire record at 1 h resolution is 1.7 ‰). Only the synoptic scale variability is well expressed in

396   the records of $\delta^{18}O_v$ and d-excess$_v$ with an anticorrelation between both parameters when

397   looking at the 2-year series at hourly resolution ($R^2 = 0.61$ with R^2 being the coefficient of

398   determination for a linear regression). Moreover, $\delta^{18}O_v$ is most of the time correlated with water

399   vapor mixing ratio ($R^2 = 0.55$ for the 2-year series at hourly resolution).

400   There are a few exceptions to the general correlation between water vapor $\delta^{18}O$ and water vapor

401   mixing ratio as illustrated in Figure 3. Short periods of a few days are associated with a decrease

402   of the correlation coefficient, R estimated from the correlation between $\delta^{18}O_v$ and q_v (R is

403   calculated continuously from hourly records on an 8-day moving window). The periods of low

404   R are also often characterized by a negative peak of several ‰ in $\delta^{18}O_v$, which is not visible in

405   the d-excess$_v$. During these $\delta^{18}O_v$ excursions, the general anti-correlation between $\delta^{18}O_v$ and d-

406   excess$_v$ hence also breaks down. Our study mostly focuses on the 11 most prominent abrupt

407   events highlighted in the $\delta^{18}O_v$ record (only 10 visible on Figure 3 because of the scale). The

408   11 most abrupt events occurring when correlation coefficient R between $\delta^{18}O_v$ and d-excess$_v$ is

409   larger than -0.5 are associated with $\delta^{18}O_v$ negative excursion larger than 3 ‰ (at 6h resolution)

410   over a period of less than 24 h, the length of the event being measured between the mid-slopes

411   of the decrease and subsequent increase of the $\delta^{18}O_v$. The 11 selected negative excursions occur

412   at a rate larger than -0.5‰ h^{-1} and the $\delta^{18}O_v$ increase at the end of each excursion has an

413   amplitude larger than half the amplitude of the corresponding initial decrease.

414

415   **3.2 Model-data comparison**

416

417
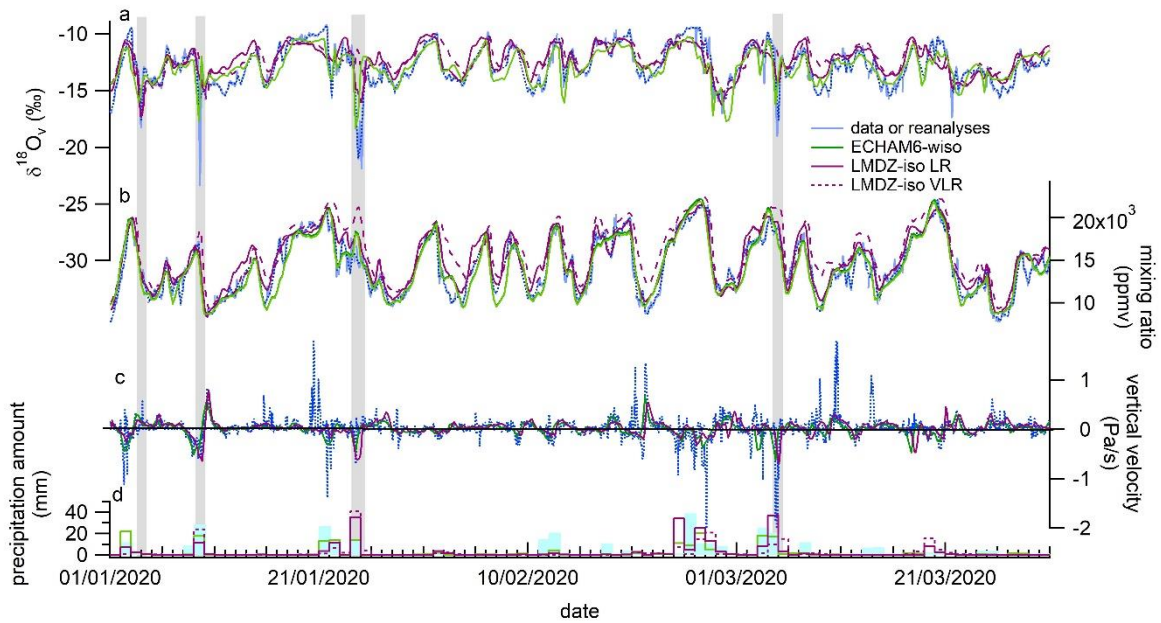
Figure 4: Model-measurement comparison (January – March 2020); a- $\delta^{18}O_v$ (light blue for

data on hourly average, dotted dark blue for data resampled at a 6-hour resolution); b- water

vapor mixing ratio from our data set; c- vertical velocity; d- Precipitation amount. The grey

shaded areas highlight the negative $\delta^{18}O_v$ excursions as defined in 3.1.3 (note that in this figure

the excursions of the 3rd and 9th of January 2020 are distinct while the distinction could not be

done on Figure 3 because of the scale).

We selected a 3-month period (January to March 2020) for the comparison between our dataset

and the outputs of the ECHAM6-wiso and LMDZ-iso models. This period has been selected

for display because it encompasses 4 out the 11 negative excursions of $\delta^{18}O_v$, but the extended

comparison over the whole 2 years period is displayed in Figure A1. There is an overall

agreement between the measured and modelled $\delta^{18}O_v$ and water vapor mixing ratio (Figure 4).

The best agreement over the 3-month series is obtained with the ECHAM6-wiso and LMDZ-

iso (LR) models ($R^2 = 0.59 – 0.6$ and $0.87 - 0.90$ respectively for $\delta^{18}O_v$ and water vapor mixing

ratio series) while a slightly less good agreement is observed with the VLR simulation of the

LMDZ-iso model ($R^2 = 0.49$ and 0.79 respectively for $\delta^{18}O_v$ and water vapor mixing ratio

series). The same observation can be done on the entire 2-year time series. We also compare

the precipitation amount modelled by ECHAM6-wiso and LMDZ-iso to the precipitation

amount measured by the MeteoFrance weather station. The correlation between modeled and

measured precipitation is close to zero for LMDZ-iso ($R^2 = 0.08 – 0.13$ for VLR - LR) while

there is a better agreement when comparing measured precipitation amount to outputs of

439   ECHAM6-wiso ($R^2 = 0.45$). Finally, when focusing on the short term negative $\delta^{18}O_v$ excursions

440   (Figures 4 and A1), they are in general more strongly expressed in the measurement time series

441   than in the model series. Part of this disagreement can be explained by the fact that the $\delta^{18}O_v$

442   record has a higher temporal resolution (1h) than the model outputs (3h for LMDZ-iso and 6h

443   for ECHAM6-wiso). However, when interpolating the $\delta^{18}O_v$ record at a 6h resolution (dotted

444   dark blue), the negative excursions are still clearly visible while not captured by the LMDZ-iso

445   model (Figure 4 and Table 1). When looking at the whole 2-year series, the LMDZ-iso VLR

446   simulation fails to reproduce most of these $\delta^{18}O_v$ excursions (only the negative excursion of 3rd

447   January, 2020 is reproduced) while the ECHAM6-wiso model is able to capture all the $\delta^{18}O_v$

448   excursions. The LMDZ-iso LR simulation produces a negative $\delta^{18}O_v$ excursion over many

449   events with a significantly lesser amplitude than in the data and in the ECHAM6-wiso model

450   (Table 1).

451

452   **4. Discussion**

453   The most remarkable pattern from this 2-year series is the succession of short negative

454   excursions of $\delta^{18}O_v$ associated with decorrelation between $\delta^{18}O_v$ and humidity, $\delta^{18}O_v$ and d-

455   excess$_v$, and which are highlighted with grey shaded areas in Figure 3, detailed in Figures 5 and

456   A2 and referenced in Table 1. These negative $\delta^{18}O_v$ excursions always occurred during low

457   pressure periods (atmospheric pressure below 1005 mbar) and we observe the presence of a

458   cold front within a distance of 100 km around Amsterdam Island in a 48h period covering the

459   time of the event (supplementary material Figure S1). The focus on the first three months of

460   the series presented in Figure 4 shows that these events are captured by ECHAM6-wiso at 0.9°

461   resolution, but not systematically by LMDZ-iso at 2x1.67° and even less by LMDZ-iso at

462   3.75x1.9° resolution. Such mismatch makes the understanding of the processes at play during

463   these events particularly important to investigate to further improve the performances of

464   atmospheric general circulation models equipped with water isotopes. .
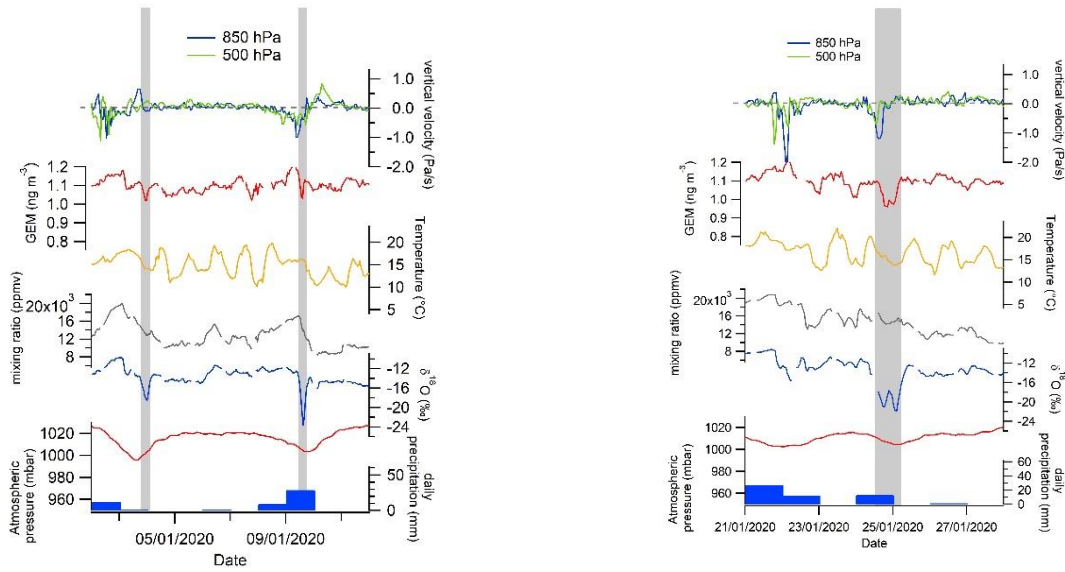
465

466 **Figure 5:** Evolution of GEM, $\delta^{18}O_v$, water vapor mixing ratio, meteorological parameters

467 (surface temperature, surface atmospheric pressure, daily precipitation) measured by the

468 MeteoFrance weather station and vertical velocity from the ERA5 reanalyses at 500 and 850

469 hPa over the three isotopic excursions of January 2020 identified on Figure 4. A focus on the

470 other excursions is provided in Figure A2.

471

472 **Table 1**: List of the 11 events associated with both loss of correlation between $\delta^{18}O_v$ and q_v,

473 $\delta^{18}O_v$ and d-excess$_v$ and negative excursions of $\delta^{18}O_v$ over 2020-2021. The amplitude of the

474 negative $\delta^{18}O_v$ anomaly is calculated from the minimum of $\delta^{18}O_v$ on the record at hourly

475 resolution (at 6h resolution). .When the calculated amplitude is smaller than 1 ‰, we indicate

476 only "-". When the vertical velocity is between -0.25 and 0.25 Pa/s, we indicate "~0".

477

478

Date of the event	Negative excursion of GEM	Low pressure (< 1005 mbar)	Rain	Relative Humidity at the surface (at minimum $\delta^{18}O_v$)	vertical velocity from reanalyses (850 hPa)	vertical velocity from reanalyses (500 hPa)	Length of the event (hours)	amplitude of the $\delta^{18}O_v$ peak in the data (‰)	amplitude of the $\delta^{18}O$ peak in ECHAM-wiso (‰)	amplitude of the $\delta^{18}O$ peak in LMDZ-iso VLR (‰)	amplitude of the $\delta^{18}O$ peak in LMDZ-iso LR (‰)
06/12/2021	Yes	Yes	Yes	82%	~0	up	3h	-6 (-5)	-2.3	-	-2
08/11/2021	Yes	Yes	No	85%	~0	~0	17h	-5.5 (-5.5)	-5	-	-4
23/06/2021	No	Yes	Yes	75%	~0	~0	10h	-5.5 (-5.4)	-6	-	-
07/06/2021	No	Yes	Yes	80%	up	~0	9h	-6.5 (-5.8)	-5.8	-	-2
08/03/2021	Yes	Yes	Yes	89%	down	up	20h	-6 (-6)	-4	-	-
09/08/2020	No data	Yes	Yes	87%	down	up	8h	-8 (-6)	-7	-	-2
10/05/2020	Small	Yes	Yes	95%	down	down	14h	-4.9 (-4)	-3	-	-3
04/03/2020	No data	Yes	Yes	98%	up	up	9h	-6.1 (-5.3)	-5	-	-
24/01/2020 (double peak)	Yes	Yes	Yes	93% and 90%	1st peak up and 2nd peak down	1st peak up and 2nd peak down	17h	-7.8 (-7.5)	-4.5	-	-3.5
09/01/2020	Yes	Yes	Yes	94%	up	up	4h	-9 (-4)	-5	-	-
03/01/2020	Yes	Yes	No	90%	down	~0	6h	-2.8 (-2.5)	-2.4	-3	-3.5

479

480 Several hypotheses can be proposed to explain the negative excursions of $\delta^{18}O_v$. The beginning

481 of these excursions is associated with a decrease of the water vapor mixing ratio and occurs in

482 most cases during a precipitation event (Table 1). These events share similarities with negative

483 $\delta^{18}O_v$ and $\delta^{18}O_p$ short events previously observed in temperate regions during a cold front

484 passage (e.g. Aemisegger et al., 2015). Three possible processes at play to explain such events

485 have already been listed in previous studies (e.g. Dütsch et al., 2016) (i) local interaction

486 between the vapor and the rain droplets (rain equilibration and rain evaporation), (ii) vertical

487 subsidence of water vapor with depleted isotopic composition, or (iii) horizontal advection

488 through the arrival of a cold front. We explore below how we can gain information on the

489 different processes using our data set, back trajectories and model-data comparison.

490

491 **4.1 $\delta^{18}O_v$ vs q_v relationship**
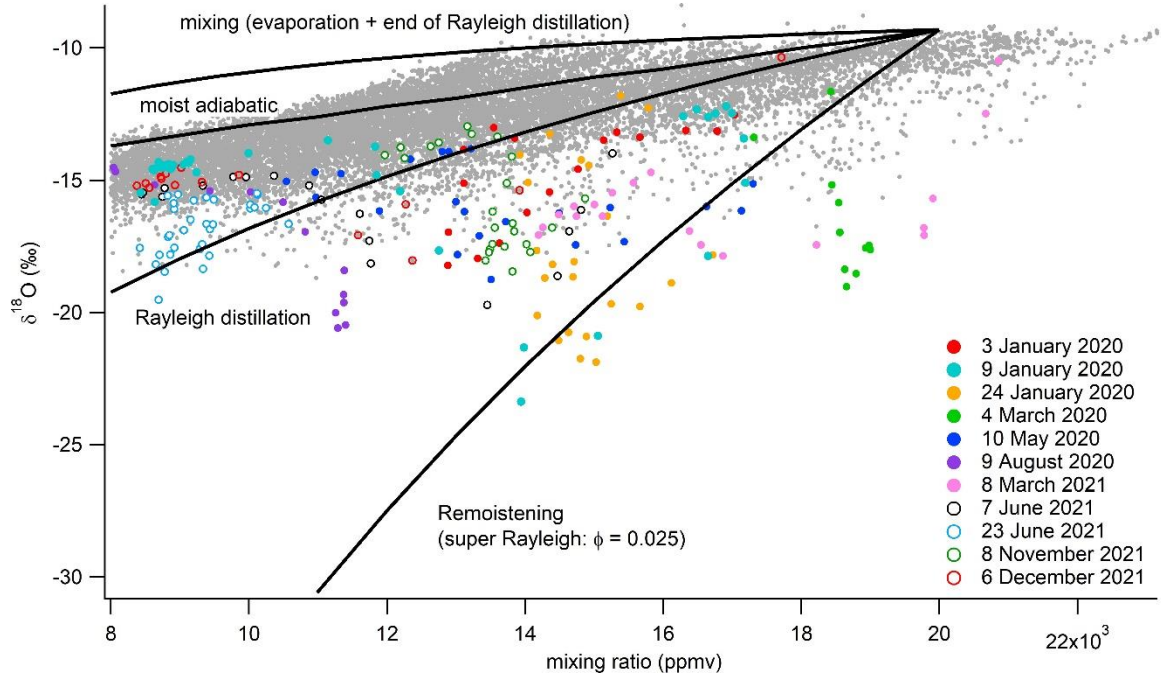
Figure 6: Relative evolution of q_v and $\delta^{18}O_v$ for the different events (colors according to the date as explained in the graph) and for the entire 2 years records (grey). The solid lines are theoretical lines whose equations are detailed in Noone (2012) for different processes (remoistening associated with exchange between rain and water vapor; Rayleigh distillation assuming that all formed condensation is removed from the cloud; moist adiabatic process assuming that liquid condensation stays in the cloud with the water vapor; mixing of water vapor from ocean evaporation around Amsterdam Island and water vapor from the end of the Rayleigh distillation, i.e. high altitude water vapor). The water vapor for the calculation of Rayleigh distillation and for the evaporation above the ocean has a $q_{v,0}$ of 20,000 ppmv and a $\delta^{18}O_{v,0}$ of -9.3 ‰. The vapor at the end of the distillation line was taken with a water vapor mixing ratio of 1,000 ppmv and a $\delta^{18}O_v$ of -40 ‰.

First, to test the hypothesis of vapor-droplet interactions, we looked at the $\delta^{18}O_v$ vs q_v distribution following the approach already used by Guilpart et al. (2017) (Figure 6). We acknowledge that our approach is crude and should be taken as a first order approach since we can only look at the water vapor $\delta^{18}O_v$ vs q_v distribution in the surface layer using adapted boundary conditions while it may be more relevant to look at this relationship in the free troposphere. In general, the $\delta^{18}O_v$ vs q_v evolution lies on a curve which can be explained by condensation processes (Rayleigh distillation or reversible moist adiabatic process). However,

for the 11 events highlighted above, the water vapor $\delta^{18}O_v$ vs q_v evolution follows an evolution standing below the curve of the $\delta^{18}O_v$ vs q_v evolution observed for the rest of the series. Even if the water vapor $\delta^{18}O_v$ vs q_v evolution is rather steep, there is some resemblance with the idealized theoretical curve for remoistening initially calculated for the free troposphere (Noone, 2012) and adapted here with initial conditions corresponding to the surface water vapor isotopic composition. Remoistening is described through a modification of the equilibrium fractionation coefficient between water vapor and rain (α_e) so that the effective fractionation factor is $\alpha = (1+\phi) \times \alpha_e$, ϕ being the degree to which α deviates from equilibrium. This effective fractionation coefficient is then introduced in the Rayleigh distillation equation to deduce the link between $\delta^{18}O_v$ and mixing ratio as:

$$\delta^{18}O_v - \delta^{18}O_{v,0} = (\alpha-1) \times \ln(q_v/q_{v,0}) \qquad \text{(Eq 8)}$$

Despite the simplicity of our approach, the fact that the water vapor $\delta^{18}O_v$ vs q_v evolution lies below the idealized curve for condensation processes supports the depleting effect of vapor-rain interactions for our negative water vapor $\delta^{18}O_v$ excursions (Noone, 2012; Worden et al., 2007). Surface relative humidity remains relatively high during these events (values given in Table 1 compared to a mean value of 77 %) which favors rain-vapor diffusive exchanges. Such interpretation is also supported by the stable d-excess$_v$ during these events.

4.2 $\delta^{18}O_v$ vs GEM relationship

Second, to test the hypothesis of subsidence of air from higher altitude, GEM is used. Indeed, aircraft measurements as well as model simulations demonstrated that the upper troposphere/lower stratosphere is depleted in GEM and enriched in species composed of reactive gaseous mercury and particulate bound mercury (Lyman and Jaffe, 2012; Murphy et al., 2006; Sillman et al., 2007; Swartzendruber et al., 2006, 2008; Talbot et al., 2007, 2008). This leads to lower GEM concentrations than those usually observed when the lowest atmosphere layer is only under marine influence (Angot et al., 2014; Lindberg et al., 2007). The fact that GEM negative excursions are observed in phase with negative $\delta^{18}O_v$ excursions in most of the events (6 events on a total of 9 events with GEM data, cf Figure 5 and A2, Table 1) suggests that vertical subsidence of water vapor, $\delta^{18}O$-depleted by Rayleigh distillation and/or rain-vapor interactions, can have an influence on the observed excursions of $\delta^{18}O_v$, in agreement with the conclusion of Dütsch et al. (2016).

4.3 Back trajectories information

546 To further explore the processes leading to the decoupling of humidity and $\delta^{18}O_v$ as well as
547 sharp negative excursions of $\delta^{18}O_v$ during the 11 events identified here, we also use information
548 from the ERA5 reanalyses. In particular, the influence of atmospheric circulation (vertical and
549 horizontal advection) and moisture origin can be studied through back trajectories. The back
550 trajectories, presented here for 3 events (Figures 7, A3 and A4), confirm the information from
551 wind directions that there is no systematic change in the horizontal origin of the trajectories for
552 the different events. No systematic pattern is identified either in the vertical advection even if
553 we note that for the event of January 3rd, the average altitude of the envelope of the 5-day back
554 trajectories increases when comparing the situation before the excursion and the situation when
555 the most negative $\delta^{18}O_v$ values are reached. This observation may support the occurrence of
556 air subsidence as indicated by the GEM record for this particular event (Figure 5).
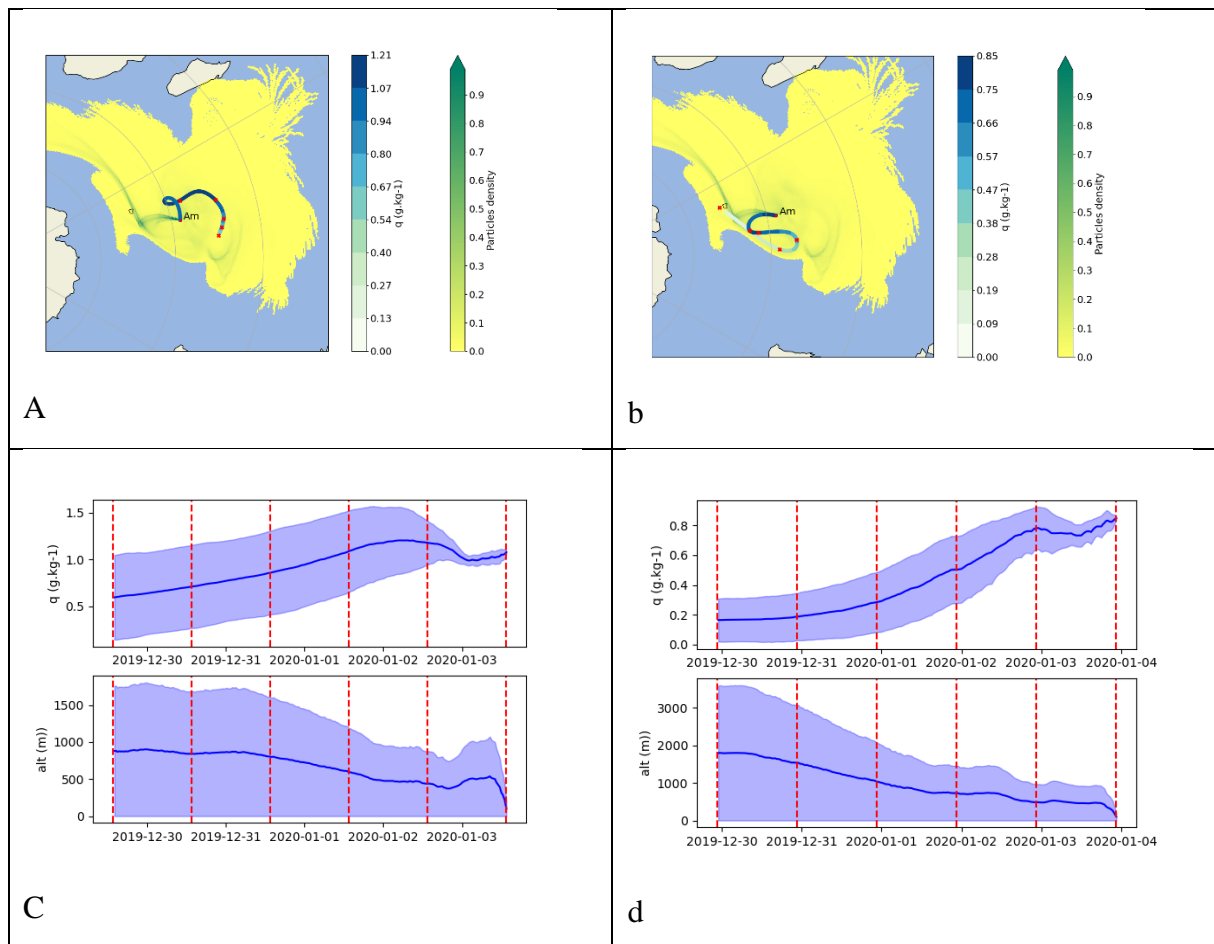
557 **Figure 7** : FLEXPART footprints of 5-day back trajectories for the event of the 3rd-4th of
558 January. (a) Latitude-longitude projection of the FLEXPART back trajectory footprints for
559 January 3rd 2020 at 13h30. The yellow to green colors on each grid point of these projections
560 represent the density of particles. The white to blue colors indicate the water vapor mixing
561 ratio along the humidity-weighted average back trajectory. Each red point indicates the

location of the average back trajectory for each of the 5 days before the date of the considered event. (b) Same as a for January 3rd 2020 at 22h30. (c) Top shows the evolution of the water vapor mixing ratio of the back trajectories for January 3rd 2020 at 13h30; bottom shows the altitude evolution of the back trajectory for January 3rd 2020 at 13h30. (d) same as (c) for January 3rd 2020 at 22h30.

The subsidence over the different events can better be studied from the vertical velocity from the ERA5 reanalyses (Figure 4 and A1). Subsidence (positive vertical velocity) is not systematically associated with negative $\delta^{18}O_v$ excursions: subsidence at either 850 hPa or 500 hPa is observed only for 5 events over 11 (Table 1). In 4 cases, there is rather an ascending movement of the atmospheric air associated with the rain event. In the other cases, there is no clear vertical movement. However, we note that when negative $\delta^{18}O_v$ excursions are not concomitant with subsidence, they occur right after an ascending movement and are generally followed by subsidence (Figures A1 and A2).

4.4 Model – data comparison and atmospheric dynamic

With the information gathered above, both subsidence and isotopic depletion associated with rain occurrence and further interaction between droplets and water vapor can explain the negative excursions of $\delta^{18}O_v$. We note however that the data gathered so far do not permit to provide a simple and unique explanation. Neither subsidence nor rain systematically occurred for each of the $\delta^{18}O_v$ excursion. Still, the fact that at least ECHAM6-wiso is able to reproduce every negative $\delta^{18}O_v$ excursion (whether they are associated or not with subsidence or rain-water vapor reequilibration) shows that not only the patterns of atmospheric water cycle are correctly reproduced (a validation which can also be performed using humidity and precipitation data) but also that the isotopic processes are correctly implemented in this model. Such abrupt $\delta^{18}O_v$ events can hence be used as a test bed of the performances of water isotopes enabled general circulation models.

To further explore the $\delta^{18}O_v$ data-model comparison and associated processes, we compare the performances of the ECHAM6-wiso and the LMDZ-iso models over the first months of 2020 in terms of atmospheric dynamics (Figures 4 and A1). First and as expected because of the nudging, the two models reproduce rather well the evolution of the vertical velocity of the ERA5 reanalyses with a stronger ascent for the model predicting the strongest precipitation amount (e.g. LMDZ-iso for January 24th 2020). The event of January 3rd is the only one

reproduced by both ECHAM6-wiso and the two versions of the LMDZ-iso model: the three simulations show a clear subsidence over the isotopic event and a clear negative $\delta^{18}O_v$ excursion. For the other events, neither LMDZ-iso nor ECHAM6-wiso show a clear signal of subsidence neither at 500 nor at 850 hPa (Figures 4 and A1). However, the horizontal distribution of vertical velocity obtained with ECHAM6-wiso and LMDZ-iso are significantly different (Figure 8 for the event of the 9th of January, supplementary material Figures S2 and S3 for the other events). While the LMDZ-iso modelled vertical velocity displays a rather strong homogeneity on the vertical axis, ECHAM6-wiso modelled vertical velocity highlights subsidence of air below the ascending column at the exact location of the negative $\delta^{18}O_v$ anomaly (Figure 8c). This subsidence of depleted $\delta^{18}O_v$ below the ascending column is responsible for the sharp negative $\delta^{18}O_v$ excursion in the ECHAM6-wiso model. The fact that subsidence of air occurs just below uplifted air, at the limit between ascendance and subsidence (Figure 8j and Supplementary Material Figure S4), permits to reconcile the GEM data suggesting subsidence and the sign of the vertical velocity of the ERA5 reanalyses at Amsterdam Island. Since the isotope implementation was done similarly in the two models, the reason why the LMDZ-iso model does not reproduce the water isotopic anomaly is its too coarse resolution as also supported by the comparison between performances of the LMDZ-iso model at low resolution and very low resolution for the event of the 24th of January (Table 1 and Figure 4). As already pointed by Ryan et al. (2000), a fine resolution is necessary to correctly simulate front dynamics and we extend this result here to the high resolution temporal patterns of surface $\delta^{18}O_v$.

4.5 Synthesis

Figure 9 summarizes the proposed mechanism for negative $\delta^{18}O_v$ excursions as inferred from our data – model comparison when there is a clear rain event. A rain event is associated with a strong ascending column in which $\delta^{18}O_v$ is depleted by progressive precipitation during the ascent and by interaction between rain and water vapor. This ascending column is coupled to the subsidence of $\delta^{18}O_v$ depleted air at the rear of the event, which is pushed toward Amsterdam Island through a south west advection of cold air.

626 a

627 d

628 g
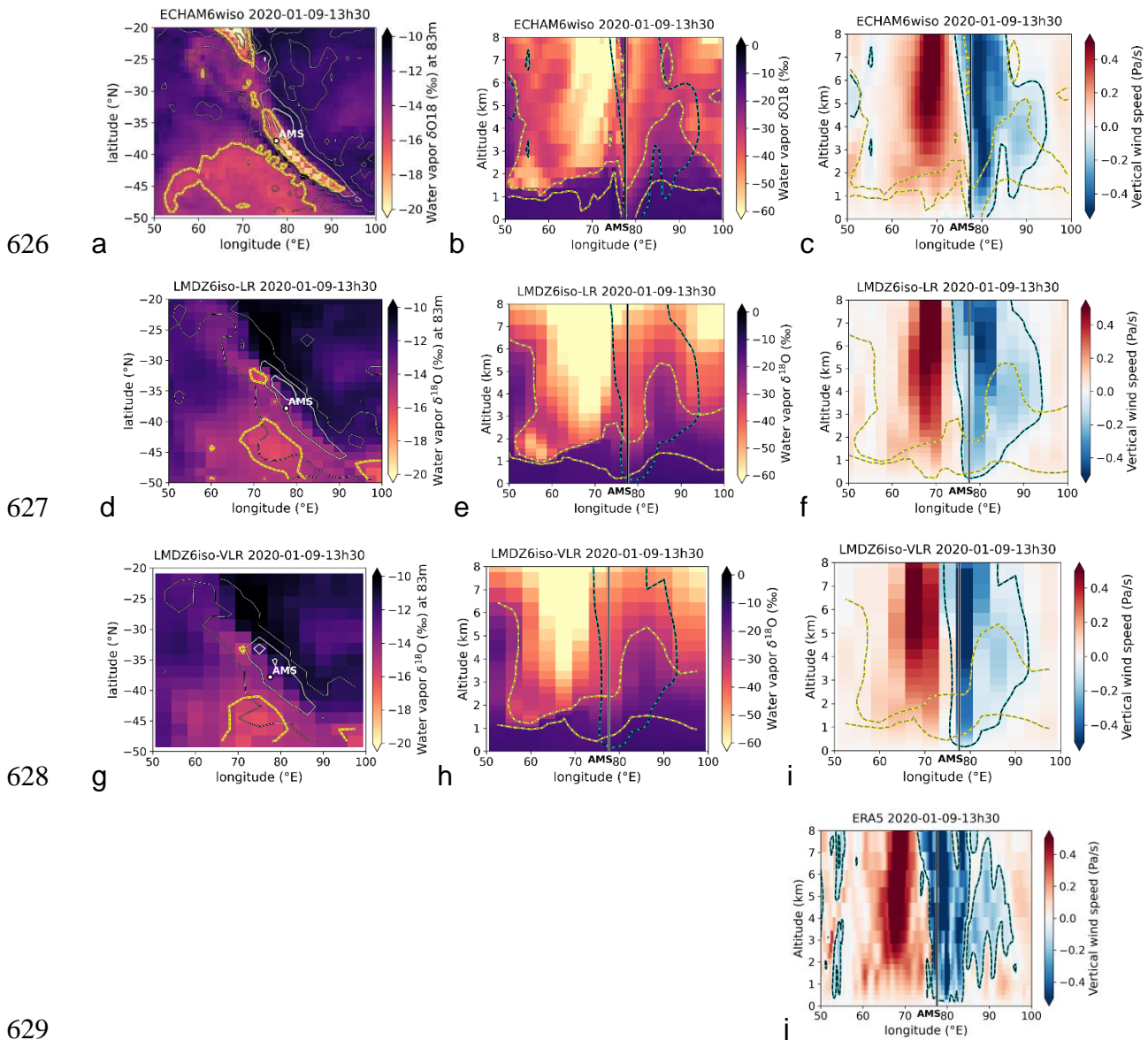
629

630

631 **Figure 8:** Pattern of the modelled $\delta^{18}O_v$ and vertical velocity for the event of January 9th 2020.

632 (a) low level (~83 m) contourplot of $\delta^{18}O_v$ in a latitude vs longitude plot, the yellow line

633 indicates the -15‰ level and grey contours indicate precipitation contours at 0.5, 10, and 50

634 mm day^{-1} (thin, medium and thick lines respectively); (b) $\delta^{18}O_v$ evolution in an altitude vs

635 longitude plot, the yellow lines indicate the $\delta^{18}O_v$ levels at -30 and -15 ‰, the blue one plots

636 the contour of –0.05 Pa s^{-1} vertical velocity (ascendance) and the vertical black line denotes

637 Amsterdam Island longitude; (c) vertical velocity in an altitude vs longitude plot with similar

638 lines as in (b) ; (a), (b) and (c) are drawn using outputs of the ECHAM6-wiso model ; (d), (e)

639 and (f) are the same as (a), (b) and (c) but obtained from the LMDZ-iso model at low resolution

640 (LR) ; (g), (h) and (i) are the same as (a), (b) and (c) but obtained from the LMDZ-iso model at

 very low resolution (VLR); (j) shows the vertical velocity in an altitude vs longitude plot from
642 ERA5.

643

644
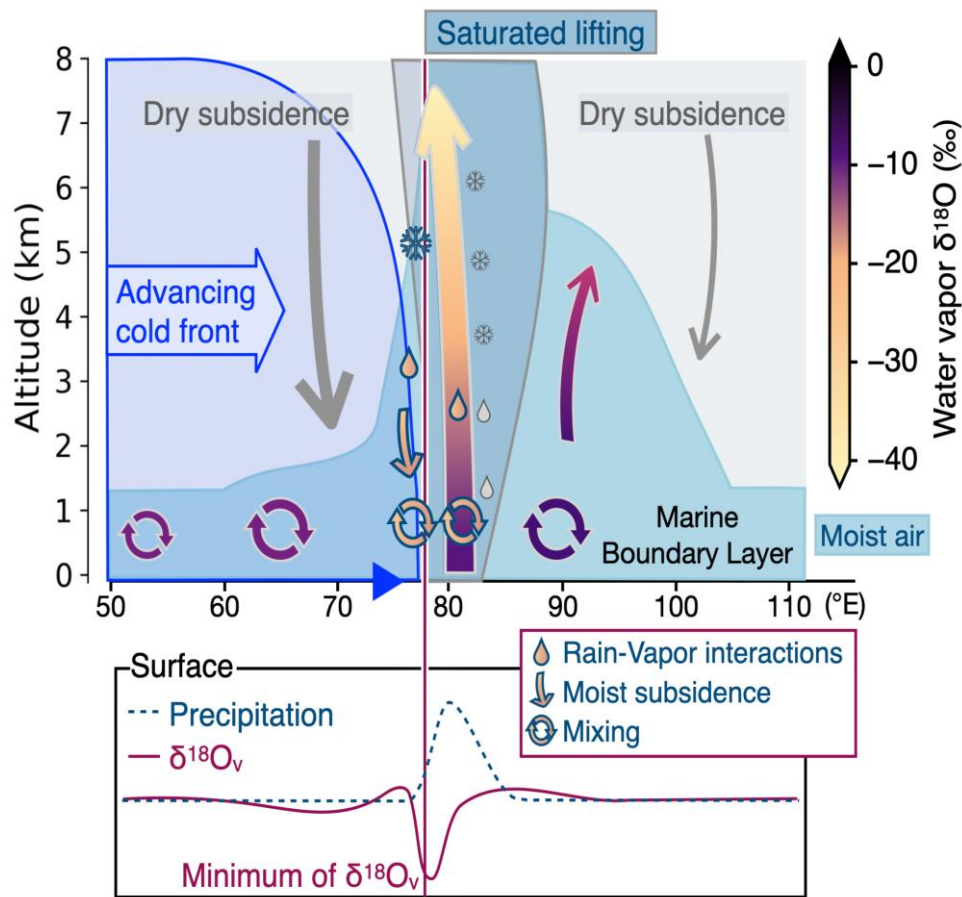
Figure 9: Scheme of the mechanism explaining the sharp negative excursion of $\delta^{18}O_v$ recorded
at the surface for cold front events associated with precipitation. The scheme is based on the
profile modelled by ECHAM6-wiso for event of January 9th 2020 (see supplementary material
Figure S5). The top panel show the altitude vs longitude dynamics of air masses with vertical
saturated lifting in the center and subsidence at the rear of the lifting. The bottom panel shows
the associated evolution of $\delta^{18}O_v$ and precipitations on the same longitude scale than on the
upper panel.

5. Conclusion

We presented here the first water vapor isotopic record over 2 years on Amsterdam Island. The
water vapor isotopic variations follow at first order the variations of water vapor mixing ratio
as expected for such a marine site. Superimposed to this variability, we have evidenced 11

periods of a few hours characterized by the occurrence of one or two abrupt negative excursions of $\delta^{18}O_v$ while the correlation between $\delta^{18}O_v$ and water vapor mixing ratio does not hold. These negative excursions are often occurring toward the end of precipitation events. They are most of the time characterized by a decrease in water vapor mixing ratio. Representation of these short events is a challenge for the atmospheric components of Earth System Models equipped with water isotopes and we found that the ECHAM6-wiso model was able to reproduce most of the sharp negative $\delta^{18}O_v$ excursions while the LMDZ-iso model at low (very low) resolution was only able to reproduce 7 (1) of the negative excursions. The good agreement between modeled and measured $\delta^{18}O_v$ when using ECHAM6-wiso validates the physics processes within the ECHAM6-wiso model as well as the implemented physics of water isotopes.

Using previous modeling studies as well as information provided by (1) the confrontation with other data sources (GEM, meteorology) obtained in parallel on this site, (2) back trajectory analyses and (3) the outputs of the two models ECHAM6-wiso and LMDZ-iso, we conclude that the most plausible explanations for such events are rain-vapor interactions and subsidence at the rear of a precipitation event. Both can be combined, since rain vapor interactions can help maintaining moist conditions in subsidence regions.

This study highlights the added value of combining different data from an atmospheric observatory to understand the dynamics of the atmospheric circulation. These 2-year records are also a good benchmark for model evaluation. We have especially shown that the isotopic composition of water vapor measured at the surface is a powerful tool to identify aspects to be improved in the atmospheric component of the Earth system models. In our case, we used it to test different horizontal resolutions which influence the representativity of the vertical dynamics and have important implication in the simulation of surface variations of water vapor $\delta^{18}O_v$. Our study highlights the importance to have high-resolution models (e.g. mesoscale models) equipped with isotopes to further study such abrupt isotopic events.

Appendices:
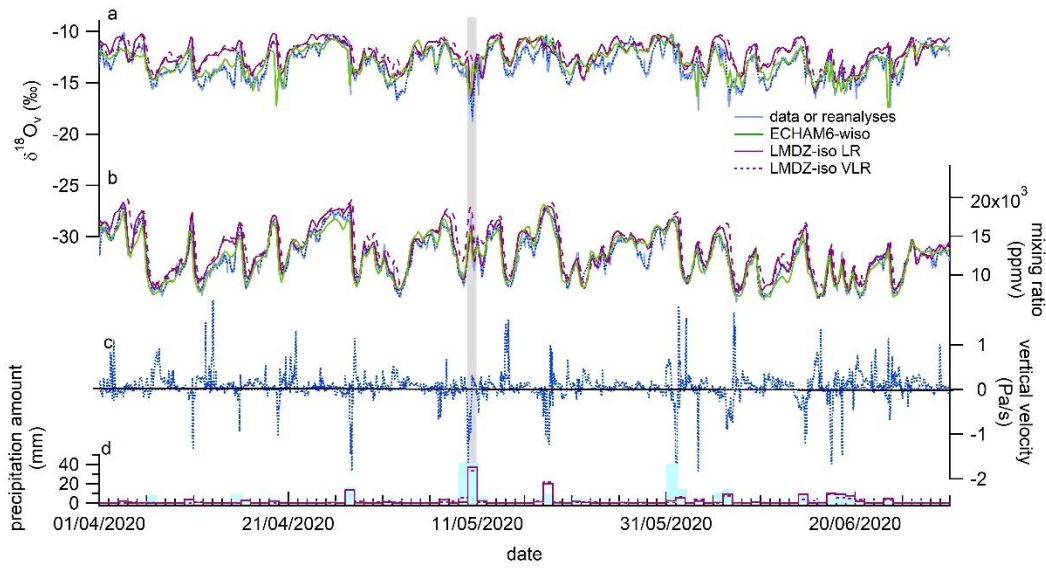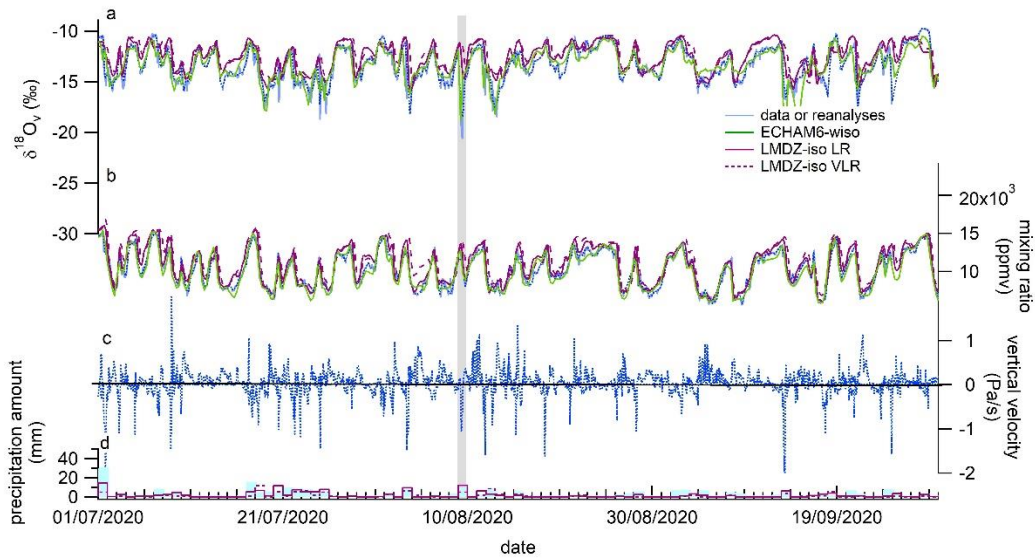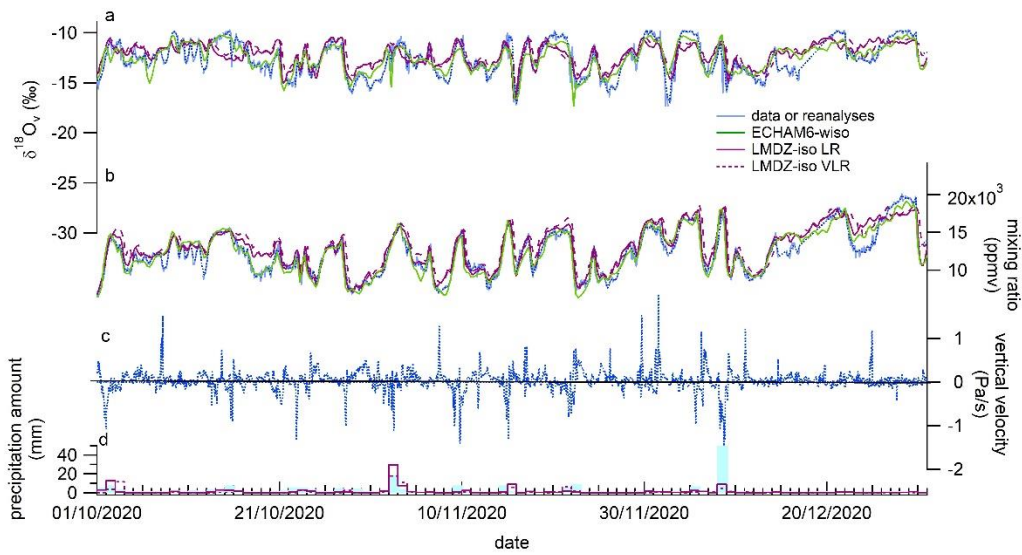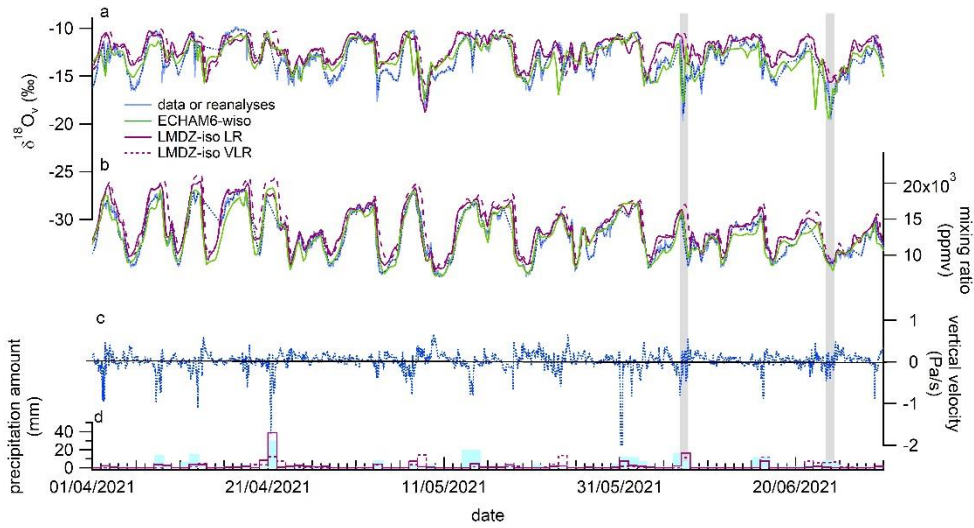
690
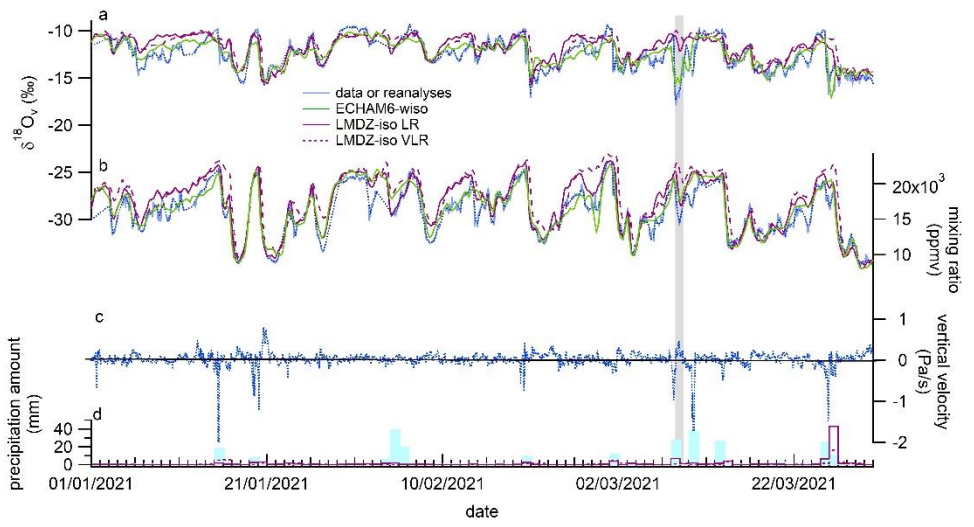
691

692
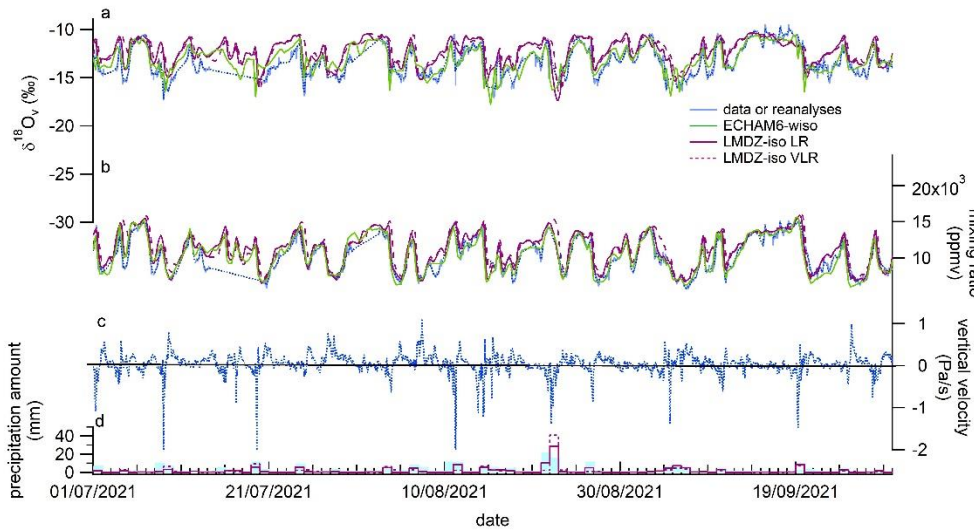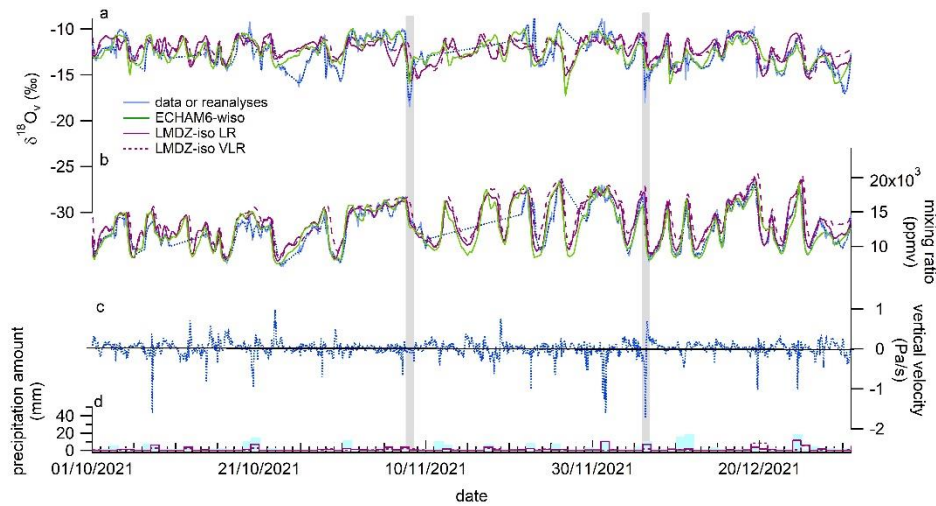
693
694
695
696 **Figure A1:** Model-measurement comparison (April 2020 – December 2021); a- $\delta^{18}O_v$ (light blue for
697 data on hourly average, dark blue for data resampled at a 6-hour resolution); b- water vapor mixing ratio
698 from our data set; c- vertical velocity; d- Precipitation amount. The grey shadings highlight the negative
699 $\delta^{18}O_v$ excursions.
700

701

702

703
704
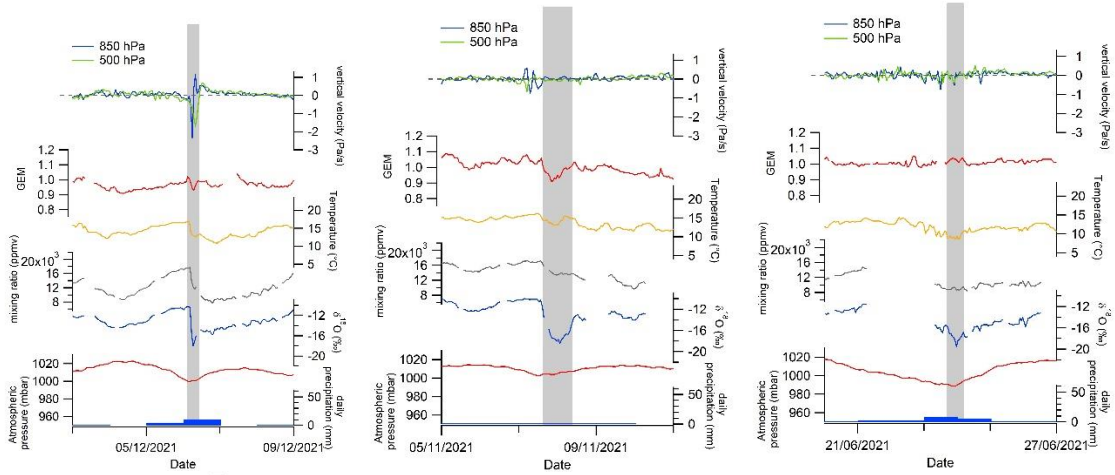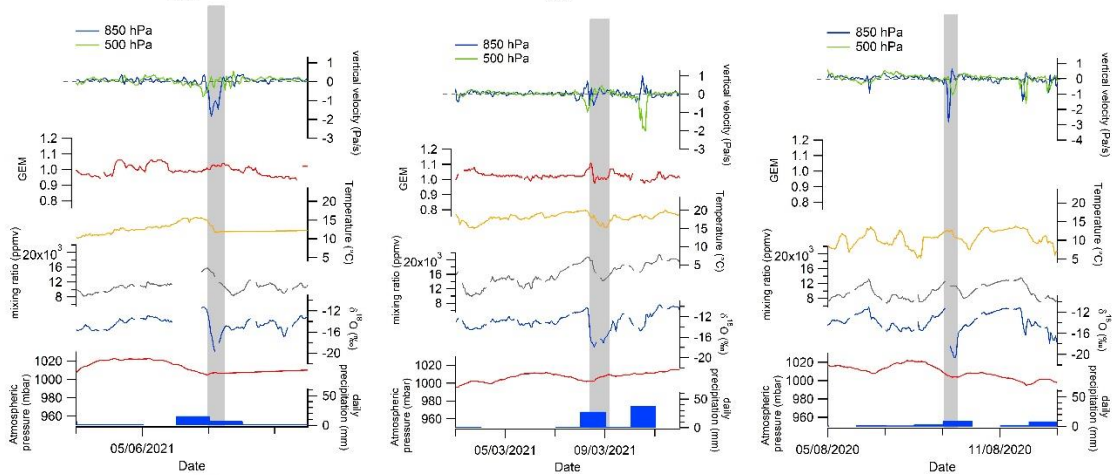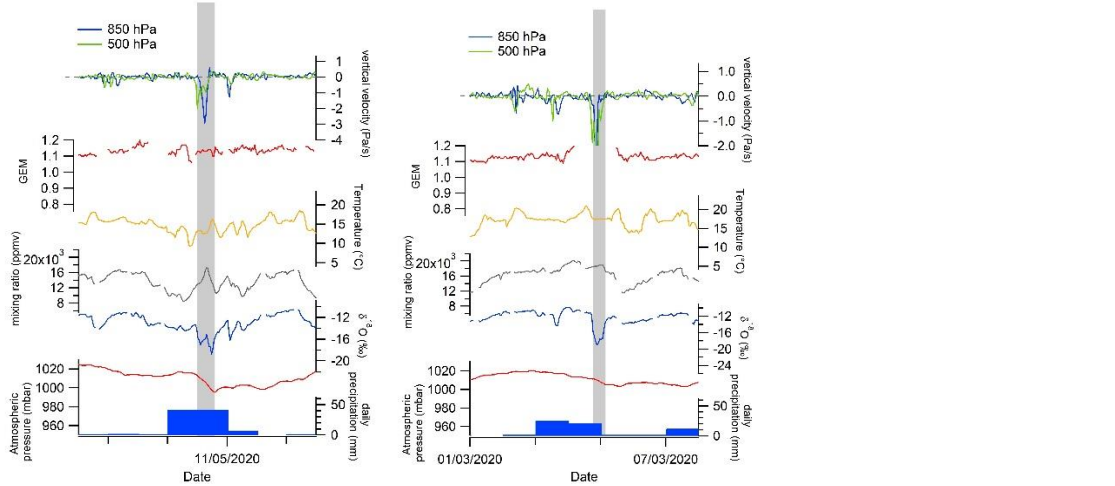
Figure A2 : Evolution of GEM, $\delta^{18}O_v$, water vapor mixing ratio, meteorological parameters (surface temperature, surface atmospheric pressure, daily precipitation) measured by the MeteoFrance weather station and vertical velocity from the ERA5 reanalyses at 500 and 850 hPa over the isotopic excursions between March 2020 and December 2021.

709

710

711
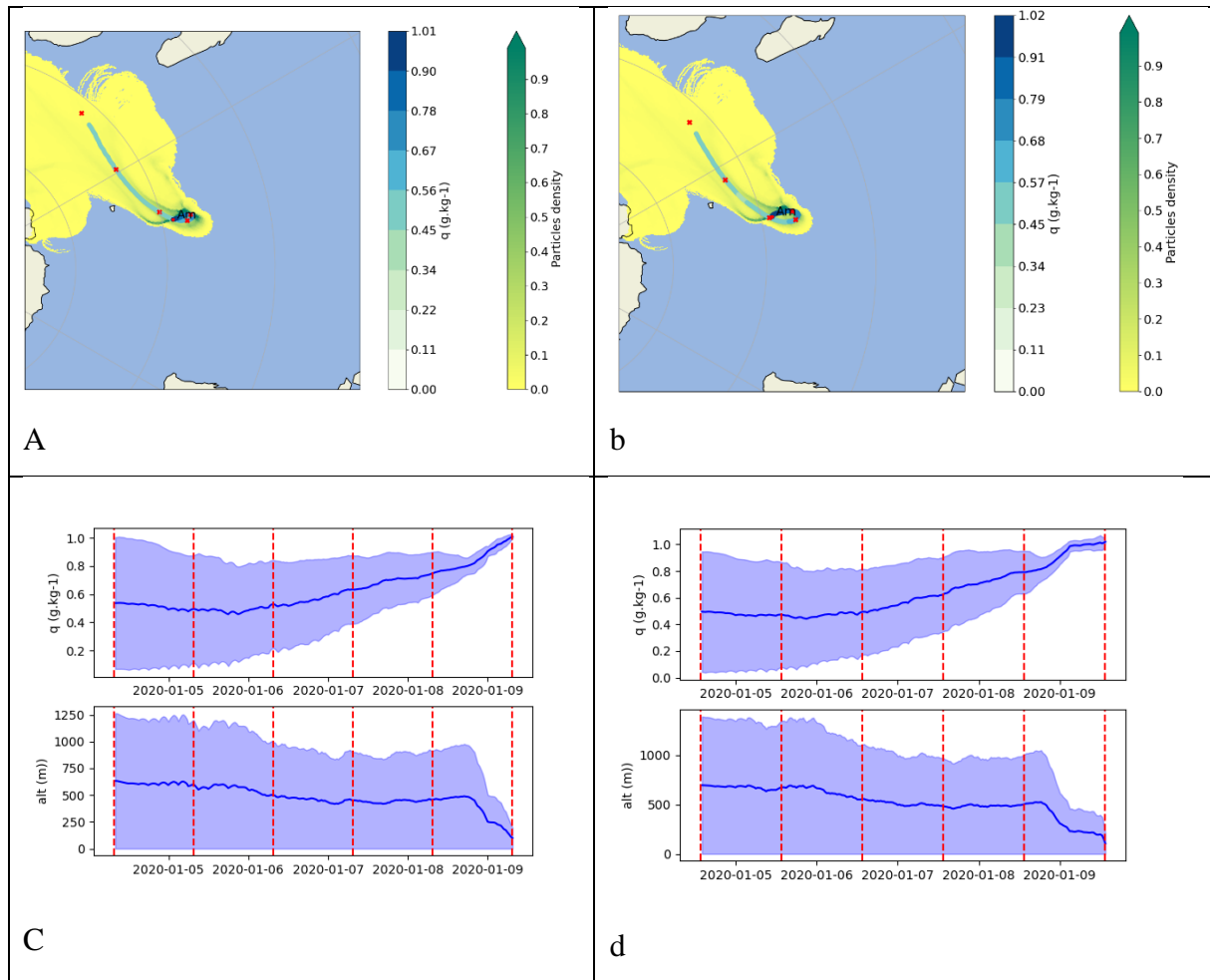
Figure A3: FLEXPART footprints of 5-day back trajectories for the event of January 9th 2020.
(a) Latitude-longitude projection of the FLEXPART back trajectory footprint for January 9th
2020 at 7h30. The yellow to green colors on each grid point of these projections represent the
density of particles. The white to blue colors indicate the water vapor mixing ratio on the
humidity weighted average back-trajectory. Each red point indicates the location of the average
back-trajectory for each of the 5 days before the date of the considered event. (b) Same as a for
January 9th 2020 at 13h30. (c) Top shows the evolution of the water vapor mixing ratio of the
back trajectories for January 9th 2020 at 7h30; bottom shows the altitude evolution of the back
trajectory for January 9th 2020 at 7h30. (d) same as (c) for January 9th 2020 at 13h30.

721

722
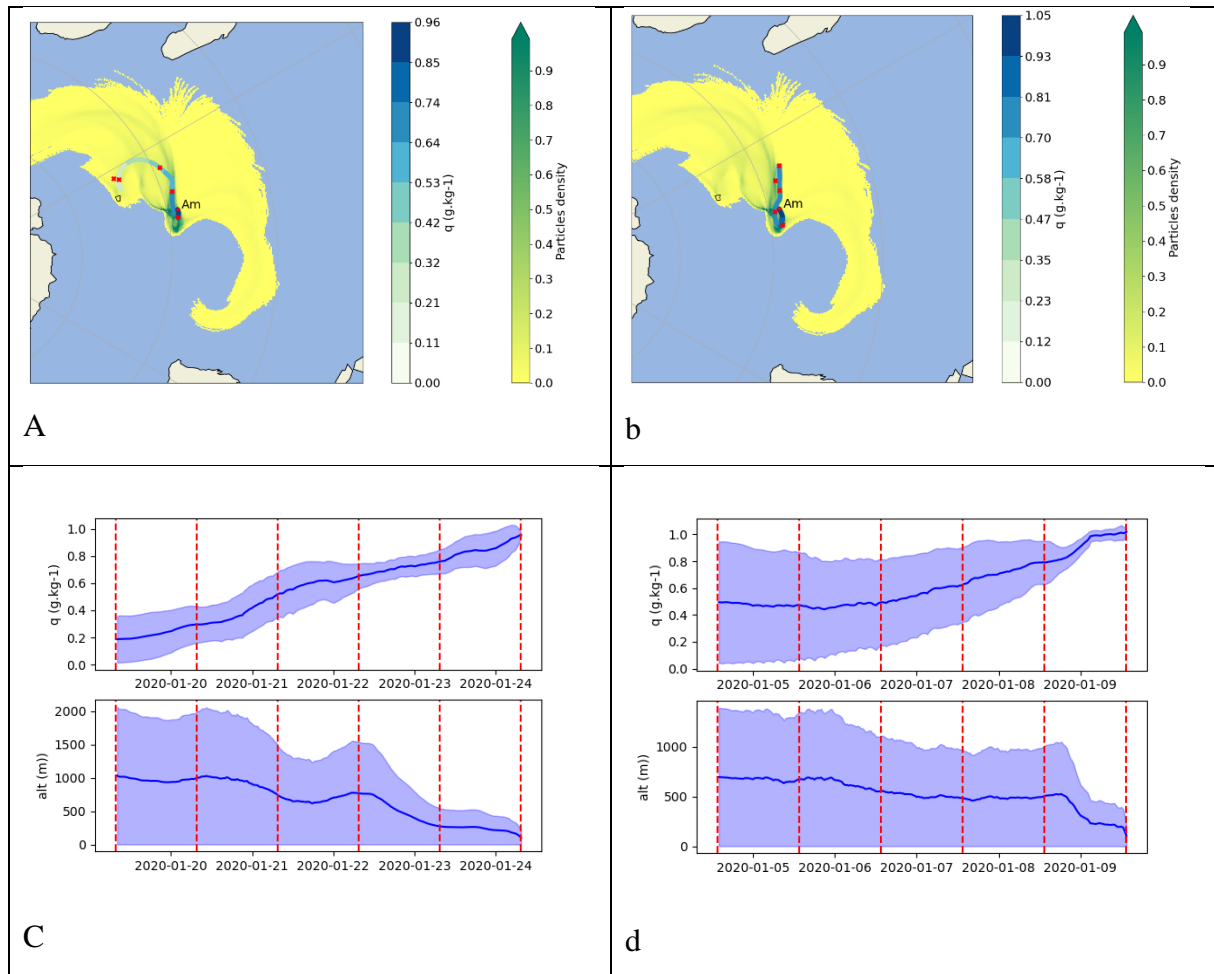
Figure A4: FLEXPART footprints of 5-day back trajectories for the event of January 21st 2020.
(a) Latitude-longitude projection of the FLEXPART back trajectory footprint for January 21st
2020 at 7h30. The yellow to green colors on each grid point of these projections represent the
density of particles. The white to blue colors indicate the water vapor mixing ratio on the
humidity weighted average back-trajectory. Each red point indicates the location of the average
back-trajectory for each of the 5 days before the date of the considered event. (b) Same as a for
January 21st 2020 at 13h00. (c) Top shows the evolution of the water vapor mixing ratio of the
back trajectories for January 21st 2020 at 7h30; bottom shows the altitude evolution of the back
trajectory for January 21st 2020 at 7h30. (d) same as (c) for January 21st 2020 at 13h00.

Data availability: AMS L2 GEM data (https://doi.org/10.25326/168) are freely available
(Magand and Dommergue, 2022) at https://gmos.aeris-data.fr/ from national GMOS-FR

website data portal coordinated by IGE (Institut des Géosciences de l'Environnement, Grenoble, France; technical PI: Olivier Magand) with the support of the French national AERIS-SEDOO partners, data and services center for the atmosphere (last access: 08 December 2022). Hg species measurements belong to international monitoring networks (http://www.gos4m.org/). Water isotopic data and modeling outputs are available on the Zenodo platform (https://zenodo.org/record/8164392; https://zenodo.org/record/8160871).

Acknowledgements: We deeply thank all overwintering staff at AMS and the French Polar Institute Paul-Emile Victor (IPEV) staff and scientists who helped with the setup and maintenance of the experiment at AMS in the framework of the GMOStral-1028 IPEV program, the ICOS-416 program and the ADELISE-1205 IPEV program. Amsterdam Island Hg0 data, accessible in national GMOS-FR website data portal were collected via instruments coordinated by the IGE-PTICHA technical platform dedicated to atmospheric chemistry field instrumentation. GMOS-FR data portal is maintained by the French national center for Atmospheric data and services AERIS, which is acknowledged by the authors. The LMDZ-iso simulation were performed thanks to granted access to the HPC resources of IDRIS under the allocations 2022-AD010114000 and 2022-AD010107632R1 and made by GENCI. We deeply thank Sébastien Nguyen (CEA, LSCE) for his help and support in running LMDZiso simulation.

Funding: This work benefited from the IPSL-CGS EUR and was supported by a grant from the French government under the Programme d'Investissements d'avenir, reference ANR-11-IDEX-0004-17-EURE-0006, managed by the Agence Nationale de la Recherche. This project has also been supported by the LEFE IMAGO project ADELISE. Amsterdam Island GEM data, accessible in national GMOS-FR website data portal have been collected with funding from European Union 7th Framework Programme project Global Mercury Observation System (GMOS 2010-2015 Nr. 26511), the French Polar Institute IPEV via GMOStral-1028 IPEV program since 2012, the LEFE CHAT CNRS/INSU (TOPMMODEL project, Nr. AO2017-984931) and the H2020 ERA-PLANET (Nr. 689443) iGOSP program. This work is part of the AWACA project that has received funding from the European Research Council (ERC) under the European Union's Horizon 2020 research and innovation programme (Grant agreement No. 951596). The ERA5 reanalyses files for the ECHAM6-wiso nudging have been provided by the German Climate Computing Center (DKRZ). The ECHAM6-wiso simulations have been performed with support of the Alfred Wegener Institute (AWI) supercomputing centre.

772

Author contributions: AL designed the study and analyzed the data together with FV, CS, EF, OM. OC installed the water vapor isotopic analyzer in Amsterdam Island and OJ was in charge of the data calibration. BM and FP performed the measurements of the isotopic composition of the precipitation samples. CA analyzed the modeling outputs, realized most of the simulations and performed model-data analyses. CLDS performed the back trajectory analyses with help from MC. OM, AD and YB provided expertise on GEM analyses and interpretation. AC, CR, ND and MW provided model simulations. AL wrote the paper with contribution of all coauthors.

Competing interests: One of the coauthors (AD) is a member of the editorial board of Atmospheric Chemistry and Physics.

References

Aemisegger, F., Sturm, P., Graf, P., Sodemann, H., Pfahl, S., Knohl, A., and Wernli, H.: Measuring variations of d18O and d2H in atmospheric water vapour using two commercial laser-based spectrometers: an instrument characterisation study, Atmospheric Measurement Techniques, 5, 1491–1511, https://doi.org/10.5194/amt-5-1491-2012, 2012.

Aemisegger, F., Spiegel, J., Pfahl, S., Sodemann, H., Eugster, W., and Wernli, H.: Isotope meteorology of cold front passages: A case study combining observations and modeling, Geophysical Research Letters, 42, 5652–5660, 2015.

Angot, H., Barret, M., Magand, O., Ramonet, M., and Dommergue, A.: A 2-year record of atmospheric mercury species at a background Southern Hemisphere station on Amsterdam Island, Atmospheric Chemistry and Physics, 14, 11461–11473, 2014.

Angot, H., Dion, I., Vogel, N., Legrand, M., Magand, O., and Dommergue, A.: Multi-year record of atmospheric mercury at Dumont d'Urville, East Antarctic coast: continental outflow and oceanic influences, Atmospheric Chemistry and Physics, 16, 8265–8279, 2016.

Ansari, M. A., Noble, J., Deodhar, A., and Kumar, U. S.: Atmospheric factors controlling the stable isotopes (δ18O and δ2H) of the Indian summer monsoon precipitation in a drying region of Eastern India, Journal of Hydrology, 584, 124636, 2020.

Arias, P., Bellouin, N., Coppola, E., Jones, R., Krinner, G., Marotzke, J., Naik, V., Palmer, M., Plattner, G.-K., Rogelj, J., and others: Climate Change 2021: the physical science basis. Contribution of Working Group I to the Sixth Assessment Report of the Intergovernmental Panel on Climate Change; technical summary, 2021.

Bailey, A., Aemisegger, F., Villiger, L., Los, S. A., Reverdin, G., Quiñones Meléndez, E., Acquistapace, C., Baranowski, D. B., Böck, T., Bony, S., Bordsdorff, T., Coffman, D., de Szoeke, S. P., Diekmann, C. J., Dütsch, M., Ertl, B., Galewsky, J., Henze, D., Makuch, P., Noone, D., Quinn, P. K., Rösch, M., Schneider, A., Schneider, M., Speich, S., Stevens, B., and Thompson, E. J.: Isotopic measurements in water vapor, precipitation, and seawater during EUREC[4]A, Earth System Science Data, 15, 465–495, https://doi.org/10.5194/essd-15-465-2023, 2023.

Benetti, M., Reverdin, G., Pierre, C., Merlivat, L., Risi, C., Steen-larsen, H. C., and Vimeux, F.: Journal of Geophysical Research : Atmospheres during evaporation, 584–593, https://doi.org/10.1002/2013JD020535.Received, 2014.

Benetti, M., Aloisi, G., Reverdin, G., Risi, C., and Sèze, G.: Importance of boundary layer mixing for the isotopic composition of surface vapor over the subtropical North Atlantic Ocean, Journal of Geophysical Research: Atmospheres, 120, 2190–2209, 2015.

Bhattacharya, S. K., Sarkar, A., and Liang, M.-C.: Vapor isotope probing of typhoons invading the Taiwan region in 2016, Journal of Geophysical Research: Atmospheres, 127, e2022JD036578, 2022.

Bloom, N. and Fitzgerald, W. F.: Determination of volatile mercury species at the picogram level by low-temperature gas chromatography with cold-vapour atomic fluorescence detection, Analytica Chimica Acta, 208, 151–161, 1988.

Bonne, J. L., Behrens, M., Meyer, H., Kipfstuhl, S., Rabe, B., Schönicke, L., Steen-Larsen, H. C., and Werner, M.: Resolving the controls of water vapour isotopes in the Atlantic sector, Nature Communications, 10, 1–10, https://doi.org/10.1038/s41467-019-09242-6, 2019.

Boucher, O., Servonnat, J., Albright, A. L., Aumont, O., Balkanski, Y., Bastrikov, V., Bekki, S., Bonnet, R., Bony, S., Bopp, L., Braconnot, P., Brockmann, P., Cadule, P., Caubel, A., Cheruy, F.,

Codron, F., Cozic, A., Cugnet, D., D'Andrea, F., Davini, P., de Lavergne, C., Denvil, S., Deshayes, J., Devilliers, M., Ducharne, A., Dufresne, J.-L., Dupont, E., Éthé, C., Fairhead, L., Falletti, L., Flavoni, S., Foujols, M.-A., Gardoll, S., Gastineau, G., Ghattas, J., Grandpeix, J.-Y., Guenet, B., Guez, E., Lionel, Guilyardi, E., Guimberteau, M., Hauglustaine, D., Hourdin, F., Idelkadi, A., Joussaume, S., Kageyama, M., Khodri, M., Krinner, G., Lebas, N., Levavasseur, G., Lévy, C., Li, L., Lott, F., Lurton, T., Luyssaert, S., Madec, G., Madeleine, J.-B., Maignan, F., Marchand, M., Marti, O., Mellul, L., Meurdesoif, Y., Mignot, J., Musat, I., Ottlé, C., Peylin, P., Planton, Y., Polcher, J., Rio, C., Rochetin, N., Rousset, C., Sepulchre, P., Sima, A., Swingedouw, D., Thiéblemont, R., Traore, A. K., Vancoppenolle, M., Vial, J., Vialard, J., Viovy, N., and Vuichard, N.: Presentation and Evaluation of the IPSL-CM6A-LR Climate Model, Journal of Advances in Modeling Earth Systems, 12, e2019MS002010, https://doi.org/10.1029/2019MS002010, 2020.

Bréant, C., Leroy Dos Santos, C., Agosta, C., Casado, M., Fourré, E., Goursaud, S., Masson-Delmotte, V., Favier, V., Cattani, O., Prié, F., Golly, B., Orsi, A., Martinerie, P., and Landais, A.: Coastal water vapor isotopic composition driven by katabatic wind variability in summer at Dumont d'Urville, coastal East Antarctica, Earth and Planetary Science Letters, 514, 37–47, https://doi.org/10.1016/j.epsl.2019.03.004, 2019.

Brooks, S.; Ren, X. R.; Cohen, M.; Luke, W. T.; Kelley, P.; Artz, R.; Hynes, A.; Landing, W.; Martos, B. Airborne vertical profiling of mercury speciation near Tullahoma, TN, USA Atmosphere 2014, 5 (3) 557– 574 DOI: 10.3390/atmos5030557.

Casado, M., Landais, A., Masson-Delmotte, V., Genthon, C., Kerstel, E., Kassi, S., Arnaud, L., Picard, G., Prie, F., Cattani, O., Steen-Larsen, H.-C., Vignon, E., and Cermak, P.: Continuous measurements of isotopic composition of water vapour on the East Antarctic Plateau, Atmospheric Chemistry and Physics, 16, https://doi.org/10.5194/acp-16-8521-2016, 2016.

Cauquoin, A. and Werner, M.: High-Resolution Nudged Isotope Modeling With ECHAM6-Wiso: Impacts of Updated Model Physics and ERA5 Reanalysis Data, Journal of Advances in Modeling Earth Systems, 13, e2021MS002532, https://doi.org/10.1029/2021MS002532, 2021.

Cauquoin, A., Werner, M., and Lohmann, G.: Water isotopes -- climate relationships for the mid-Holocene and preindustrial period simulated with an isotope-enabled version of MPI-ESM, Climate of the Past, 15, 1913–1937, https://doi.org/10.5194/cp-15-1913-2019, 2019.

Craig, H.: Isotopic Variations in Meteoric Waters, Science, 133, 1702–1703, https://doi.org/10.1126/science.133.3465.1702, 1961.

Dahinden, F., Aemisegger, F., Wernli, H., Schneider, M., Diekmann, C. J., Ertl, B., Knippertz, P., Werner, M., and Pfahl, S.: Disentangling different moisture transport pathways over the eastern subtropical North Atlantic using multi-platform isotope observations and high-resolution numerical modelling, Atmospheric Chemistry and Physics, 21, 16319–16347, https://doi.org/10.5194/acp-21-16319-2021, 2021.

Dansgaard, W.: Stable isotopes in precipitation., Tellus, 16, 436–468, 1964.

Dumarey, R., Temmerman, E., Adams, R., and Hoste, J.: The accuracy of the vapour-injection calibration method for the determination of mercury by amalgamation/cold-vapour atomic absorption spectrometry, Analytica Chimica Acta, 170, 337–340, 1985.

Durack, P. J., Taylor, K. E., Ames, S., Po-Chedley, S., and Mauzey, C.: PCMDI AMIP SST and sea-ice boundary conditions version 1.1.8, , https://doi.org/10.22033/ESGF/input4MIPs.16921, 2022.

Dütsch, M., Pfahl, S., and Wernli, H.: Drivers of $\delta 2H$ variations in an idealized extratropical cyclone, Geophysical Research Letters, 43, 5401–5408, 2016.

874   Edwards, B. A., Kushner, D. S., Outridge, P. M., Wang, F. (2021). Fifty years of volcanic mercury
875   emission research: Knowledge gaps and future directions. *Science of The Total Environment*, *757*,
876   143800. https://doi.org/10.1016/j.scitotenv.2020.143800.

878   El Yazidi, A., Ramonet, M., Ciais, P., Broquet, G., Pison, I., Abbaris, A., Brunner, D., Conil, S.,
879   Delmotte, M., Gheusi, F., and others: Identification of spikes associated with local sources in
880   continuous time series of atmospheric CO, CO_2 and CH_4, Atmospheric Measurement Techniques, 11,
881   1599–1614, 2018.

882   Eyring, V., Bony, S., Meehl, G. A., Senior, C. A., Stevens, B., Stouffer, R. J., and Taylor, K. E.:
883   Overview of the Coupled Model Intercomparison Project Phase 6 (CMIP6) experimental design and
884   organization, Geoscientific Model Development, 9, 1937–1958, https://doi.org/10.5194/gmd-9-1937-
885   2016, 2016.

886   Fain, X.; Obrist, D.; Hallar, A. G.; Mccubbin, I.; Rahn, T. High levels of reactive gaseous mercury
887   observed at a high elevation research laboratory in the Rocky Mountains Atmos. Chem.
888   Phys. 2009, 9 (20) 8049– 8060 DOI: 10.5194/acp-9-8049-2009.

890   Fitzgerald, W. F. and Gill, G. A.: Subnanogram determination of mercury by two-stage gold
891   amalgamation and gas phase detection applied to atmospheric analysis, Analytical chemistry, 51,
892   1714–1720, 1979.

893   Fogt, R. and Marshall, G.: The Southern Annular Mode: Variability, trends, and climate impacts
894   across the Southern Hemisphere, Wiley Interdisciplinary Reviews: Climate Change, 11,
895   https://doi.org/10.1002/wcc.652, 2020.

896   Fu, X., Maruszczak, N., Wang, X., Gheusi, F. and Sonke, J.: The isotopic composition of gaseous
897   elemental mercury in the free troposphere of the Pic du Midi Observatory, France. Environmental
898   Science & Technology. 50. 10.1021/acs.est.6b00033, 2016

900   Galewsky, J., Steen-Larsen, H. C., Field, R. D., Worden, J., Risi, C., and Schneider, M.: Stable
901   isotopes in atmospheric water vapor and applications to the hydrologic cycle, Reviews of Geophysics,
902   54, 809–865, 2016.

903   Gaudry, A., Ascencio, J., and Lambert, G.: Preliminary study of CO2 variations at Amsterdam Island
904   (Territoire des Terres Australes et Antarctiques Francaises), Journal of Geophysical Research: Oceans,
905   88, 1323–1329, 1983.

906   Graf, P., Wernli, H., Pfahl, S., and Sodemann, H.: A new interpretative framework for below-cloud
907   effects on stable water isotopes in vapour and rain, Atmospheric Chemistry and Physics, 19, 747–765,
908   2019.

909   Gros, V., Poisson, N., Martin, D., Kanakidou, M., and Bonsang, B.: Observations and modeling of the
910   seasonal variation of surface ozone at Amsterdam Island: 1994–1996, Journal of Geophysical
911   Research: Atmospheres, 103, 28103–28109, 1998.

912   Gros, V., Bonsang, B., Martin, D., Novelli, P., and Kazan, V.: Carbon monoxide short term
913   measurements at Amsterdam island: estimations of biomass burning emission rates, Chemosphere-
914   Global Change Science, 1, 163–172, 1999.

915   Gaffney J, Marley N. In-depth review of atmospheric mercury: sources, transformations, and potential
916   sinks. *Energy and Emission Control Technologies*. 2014;2:1-21https://doi.org/10.2147/EECT.S37038.

918   Guilpart, E., Vimeux, F., Evan, S., Brioude, J., Metzger, J., Barthe, C., Risi, C., and Cattani, O.: The
919   isotopic composition of near-surface water vapor at the Maïdo observatory (Reunion Island,

southwestern Indian Ocean) documents the controls of the humidity of the subtropical troposphere, Journal of Geophysical Research: Atmospheres, 122, 9628–9650, https://doi.org/10.1002/2017JD026791, 2017.

Gustin, M. S., Amos, H. M., Huang, J., Miller, M. B., and Heidecorn, K.: Measuring and modeling mercury in the atmosphere: a critical review, Atmos. Chem. Phys., 15, 5697–5713, https://doi.org/10.5194/acp-15-5697-2015, 2015.

Gustin, M. S., Bank, M. S., Bishop, K., Bowman, K., Brafireun, B., Chételat, J., Eckley, C. S., Hammerschmidt, C. R., Lamborg, C., Lyman, S., Martínez-Cortizas, A., Sommar, J., Tsz-Ki Tsui, M., & Zhang, T. (2020). Mercury biogeochemical cycling: A synthesis of recent scientific advances. Science of the Total Environment, 737, 139619. https://doi.org/10.1016/j.scitotenv.2020.139619.

Gworek, B., Dmuchowski, W. & Baczewska-Dąbrowska, A.H. Mercury in the terrestrial environment: a review. Environ Sci Eur **32**, 128 (2020). https://doi.org/10.1186/s12302-020-00401-x.

Henze, D., Noone, D., and Toohey, D.: Aircraft measurements of water vapor heavy isotope ratios in the marine boundary layer and lower troposphere during ORACLES, Earth Syst. Sci. Data, 14, 1811–1829, https://doi.org/10.5194/essd-14-1811-2022, 2022.

Hersbach, H., Bell, B., Berrisford, P., Hirahara, S., Horányi, A., Muñoz-Sabater, J., Nicolas, J., Peubey, C., Radu, R., Schepers, D., Simmons, A., Soci, C., Abdalla, S., Abellan, X., Balsamo, G., Bechtold, P., Biavati, G., Bidlot, J., Bonavita, M., De Chiara, G., Dahlgren, P., Dee, D., Diamantakis, M., Dragani, R., Flemming, J., Forbes, R., Fuentes, M., Geer, A., Haimberger, L., Healy, S., Hogan, R. J., Hólm, E., Janisková, M., Keeley, S., Laloyaux, P., Lopez, P., Lupu, C., Radnoti, G., de Rosnay, P., Rozum, I., Vamborg, F., Villaume, S., and Thépaut, J.-N.: The ERA5 global reanalysis, Quarterly Journal of the Royal Meteorological Society, 146, 1999–2049, https://doi.org/10.1002/qj.3803, 2020.

Hoang, C., Magand, O., Brioude, J., Dimuro, A., Brunet, C., Ah-Peng, C., Bertrand, Y., Dommergue, A., Lei, Y. D., and Wania, F.: Probing the limits of sampling gaseous elemental mercury passively in the remote atmosphere, Environ. Sci.: Atmos., 3, 268–281, https://doi.org/10.1039/D2EA00119E, 2023.

Hourdin, F., Rio, C., Grandpeix, J.-Y., Madeleine, J.-B., Cheruy, F., Rochetin, N., Jam, A., Musat, I., Idelkadi, A., Fairhead, L., Foujols, M.-A., Mellul, L., Traore, A.-K., Dufresne, J.-L., Boucher, O., Lefebvre, M.-P., Millour, E., Vignon, E., Jouhaud, J., Diallo, F. B., Lott, F., Gastineau, G., Caubel, A., Meurdesoif, Y., and Ghattas, J.: LMDZ6A: The Atmospheric Component of the IPSL Climate Model With Improved and Better Tuned Physics, Journal of Advances in Modeling Earth Systems, 12, e2019MS001892, https://doi.org/10.1029/2019MS001892, 2020.

Jiskra, M., Sonke, J. E., Obrist, D., Bieser, J., Ebinghaus, R., Myhre, C. L., Pfaffhuber, K. A., Wängberg, I., Kyllönen, K., Worthy, D., Martin, L. G., Labuschagne, C., Mkololo, T., Ramonet, M., Magand, O., and Dommergue, A.: A vegetation control on seasonal variations in global atmospheric mercury concentrations, Nature Geoscience, 11, 244–250, https://doi.org/10.1038/s41561-018-0078-8, 2018.

Jullien, N., Vignon, É., Sprenger, M., Aemisegger, F., and Berne, A.: Synoptic conditions and atmospheric moisture pathways associated with virga and precipitation over coastal Adélie Land in Antarctica, The Cryosphere, 14, 1685–1702, https://doi.org/10.5194/tc-14-1685-2020, 2020.

Koening, A.M., Magand, O., Verreyken, B., Brioude, J., Amelynck, C., Schoon, N., Colomb, A., Ramonet, M., Sha, M.K., Cammas, J.P., Sonke, J.E., Dommergue, A., 2023. Mercury in the free troposphere and bidirectional atmosphere-vegetation exchanges – Insights from Maido observatory in the southern hemisphere tropics. Atmos. Chem. Phys., 23, 1309-1328, https://doi.org/10.5194/acp-23-1309-2023

971   Lee, K.-O., Aemisegger, F., Pfahl, S., Flamant, C., Lacour, J.-L., and Chaboureau, J.-P.: Contrasting
972   stable water isotope signals from convective and large-scale precipitation phases of a heavy
973   precipitation event in southern Italy during HyMeX IOP 13: a modelling perspective, Atmospheric
974   Chemistry and Physics, 19, 7487–7506, 2019.

975   LeGrande, A. N. and Schmidt, G. A.: Global gridded data set of the oxygen isotopic composition in
976   seawater, Geophysical Research Letters, 33, 1–5, https://doi.org/10.1029/2006GL026011, 2006.

977   Leroy-Dos Santos, C., Masson-Delmotte, V., Casado, M., Fourré, E., Steen-Larsen, H. C., Maturilli,
978   M., Orsi, A., Berchet, A., Cattani, O., Minster, B., Gherardi, J., and Landais, A.: A 4.5 Year-Long
979   Record of Svalbard Water Vapor Isotopic Composition Documents Winter Air Mass Origin, Journal
980   of Geophysical Research: Atmospheres, 125, e2020JD032681-e2020JD032681,
981   https://doi.org/10.1029/2020JD032681, 2020.

982   Leroy-Dos Santos, C., Casado, M., Prié, F., Jossoud, O., Kerstel, E., Farradèche, M., Kassi, S., Fourré,
983   E., and Landais, A.: A dedicated robust instrument for water vapor generation at low humidity for use
984   with a laser water isotope analyzer in cold and dry polar regions, Atmospheric Measurement
985   Techniques, 14, 2907–2918, https://doi.org/10.5194/amt-14-2907-2021, 2021.

986   Li, C., Enrico, M., Magand, O., Araujo, B. F., Le Roux, G., Osterwalder, S., Dommergue, A.,
987   Bertrand, Y., Brioude, J., De Vleeschouwer, F., and others: A peat core Hg stable isotope
988   reconstruction of Holocene atmospheric Hg deposition at Amsterdam Island (37.8 oS), Geochimica et
989   Cosmochimica Acta, 341, 62–74, 2023.

990   Lindberg, S., Bullock, R., Ebinghaus, R., Engstrom, D., Feng, X., Fitzgerald, W., Pirrone, N., Prestbo,
991   E., and Seigneur, C.: A synthesis of progress and uncertainties in attributing the sources of mercury in
992   deposition., Ambio, 36, 19–32, 2007, https://doi.org/10.1579/0044-7447(2007)

993   Lyman, S. N.; Jaffe, D. A. Formation and fate of oxidized mercury in the upper troposphere and lower
994   stratosphere Nat. Geosci. 2012, 5 (2) 114– 117 doi: 10.1038/ngeo1353
995

996   Magand, O. and Dommergue, A.: Continuous measurements of atmospheric mercury at Maido
997   Observatory (L2), Global Mercury Observation System [data set], 2022.

998   Munksgaard, N. C., Zwart, C., Kurita, N., Bass, A., Nott, J., and Bird, M. I.: Stable isotope anatomy of
999   tropical cyclone Ita, north-eastern Australia, April 2014, PloS one, 10, e0119728, 2015.

1000   Murphy, D. M.; Hudson, P. K.; Thomson, D. S.; Sheridan, P. J.; Wilson, J. C. Observations of Mercury-
1001   Containing Aerosols. Environ. Sci. Technol. 2006, 40 (10), 3163–3167.
1002

1003   Noone, D.: Pairing Measurements of the Water Vapor Isotope Ratio with Humidity to Deduce
1004   Atmospheric Moistening and Dehydration in the Tropical Midtroposphere, Journal of Climate, 25,
1005   4476–4494, https://doi.org/10.1175/JCLI-D-11-00582.1, 2012.

1006   Pisso, I., Sollum, E., Grythe, H., Kristiansen, N. I., Cassiani, M., Eckhardt, S., Arnold, D., Morton, D.,
1007   Thompson, R. L., Groot Zwaaftink, C. D., Evangeliou, N., Sodemann, H., Haimberger, L., Henne, S.,
1008   Brunner, D., Burkhart, J. F., Fouilloux, A., Brioude, J., Philipp, A., Seibert, P., and Stohl, A.: The
1009   Lagrangian particle dispersion model FLEXPART version 10.4, Geoscientific Model Development,
1010   12, 4955–4997, https://doi.org/10.5194/gmd-12-4955-2019, 2019.

1011   Polian, G., Lambert, G., Ardouin, B., and Jegou, A.: Long-range transport of continental radon in
1012   subantarctic and antarctic areas, Tellus B: Chemical and Physical Meteorology, 38, 178–189, 1986.

1013   Risi, C., Bony, S., Vimeux, F., and Jouzel, J.: Water-stable isotopes in the LMDZ4 general circulation
1014   model: Model evaluation for present-day and past climates and applications to climatic interpretations

1015   of tropical isotopic records, Journal of Geophysical Research Atmospheres, 115,
1016   https://doi.org/10.1029/2009JD013255, 2010.

1017   Ryan, B.F., J.J. Katzfey, D.J. Abbs, C. Jakob, U. Lohmann, B. Rockel, L.D. Rotstayn, R.E. Stewart,
1018   K.K. Szeto, G. Tselioudis, and M.K. Yau, 2000: Simulations of a cold front by cloud-resolving,
1019   limited-area, and large-scale models, and a model evaluation using in situ and satellite observations.
1020   *Mon. Weather Rev.*, **128**, 3218-3235, doi:10.1175/1520-0493(2000)
1021

1022   Sciare, J., Mihalopoulos, N., and Dentener, F.: Interannual variability of atmospheric dimethylsulfide
1023   in the southern Indian Ocean, Journal of Geophysical Research: Atmospheres, 105, 26369–26377,
1024   2000.

1025   Sciare, J., Favez, O., Sarda-Estève, R., Oikonomou, K., Cachier, H., and Kazan, V.: Long-term
1026   observations of carbonaceous aerosols in the Austral Ocean atmosphere: Evidence of a biogenic
1027   marine organic source, Journal of Geophysical Research: Atmospheres, 114, 2009.

1028   Shah, V., Jacob, D. J., Thackray, C. P., Wang, X., Sunderland, E. M., Dibble, T. S., Saiz-Lopez, A., Cˇ
1029   ernušák, I., Kellö, V., astro, P. J., Wu, R., and Wang, C.: Improved Mechanistic Model of the
1030   Atmospheric Redox Chemistry of Mercury, Environ. Sci. Technol., 55, 14445–14456,
1031   https://doi.org/10.1021/acs.est.1c03160, 2021.
1032

1033   Sheu, G. R.; Lin, N. H.; Wang, J. L.; Lee, C. T.; Yang, C. F. O.; Wang, S. H. Temporal distribution and
1034   potential sources of atmospheric mercury measured at a high-elevation background station in
1035   Taiwan Atmos. Environ. 2010, 44 (20) 2393– 2400 DOI: 10.1016/j.atmosenv.2010.04.009
1036

1037   Sherwood, S. C., Bony, S., and Dufresne, J.-L.: Spread in model climate sensitivity traced to
1038   atmospheric convective mixing, Nature, 505, 37–42, https://doi.org/10.1038/nature12829, 2014.

1039   Sillman, S., Marsik, F. J., Al-Wali, K. I., Keeler, G. J., and Landis, M. S.: Reactive mercury in the
1040   troposphere: Model formation and results for Florida, the northeastern United States, and the Atlantic
1041   Ocean, Journal of Geophysical Research: Atmospheres, 112, 2007.

1042   Slemr, F., Angot, H., Dommergue, A., Magand, O., Barret, M., Weigelt, A., Ebinghaus, R., Brunke,
1043   E.-G., Pfaffhuber, K. A., Edwards, G., and others: Comparison of mercury concentrations measured at
1044   several sites in the Southern Hemisphere, Atmospheric Chemistry and Physics, 15, 3125–3133, 2015.

1045   Slemr, F., Martin, L., Labuschagne, C., Mkololo, T., Angot, H., Magand, O., Dommergue, A., Garat,
1046   P., Ramonet, M., and Bieser, J.: Atmospheric mercury in the Southern Hemisphere–Part 1: Trend and
1047   inter-annual variations in atmospheric mercury at Cape Point, South Africa, in 2007–2017, and on
1048   Amsterdam Island in 2012–2017, Atmospheric Chemistry and Physics, 20, 7683–7692, 2020.

1049   Sprovieri, F., Pirrone, N., Bencardino, M., D'amore, F., Carbone, F., Cinnirella, S., Mannarino, V.,
1050   Landis, M., Ebinghaus, R., Weigelt, A., and others: Atmospheric mercury concentrations observed at
1051   ground-based monitoring sites globally distributed in the framework of the GMOS network,
1052   Atmospheric chemistry and physics, 16, 11915–11935, 2016.

1053   Steen-Larsen, H. C., Johnsen, S. J., Masson-Delmotte, V., Stenni, B., Risi, C., Sodemann, H., Balslev-
1054   Clausen, D., Blunier, T., Dahl-Jensen, D., Elleh??j, M. D., Falourd, S., Grindsted, A., Gkinis, V.,
1055   Jouzel, J., Popp, T., Sheldon, S., Simonsen, S. B., Sjolte, J., Steffensen, J. P., Sperlich, P.,
1056   Sveinbj??rnsd??ttir, A. E., Vinther, B. M., and White, J. W. C.: Continuous monitoring of summer
1057   surface water vapor isotopic composition above the Greenland Ice Sheet, Atmospheric Chemistry and
1058   Physics, 13, 4815–4828, https://doi.org/10.5194/acp-13-4815-2013, 2013.

Steffen, A., Scherz, T., Olson, M., Gay, D., and Blanchard, P.: A comparison of data quality control protocols for atmospheric mercury speciation measurements, Journal of Environmental Monitoring, 14, 752–765, 2012.

Stevens, B., Giorgetta, M., Esch, M., Mauritsen, T., Crueger, T., Rast, S., Salzmann, M., Schmidt, H., Bader, J., Block, K., Brokopf, R., Fast, I., Kinne, S., Kornblueh, L., Lohmann, U., Pincus, R., Reichler, T., and Roeckner, E.: Atmospheric component of the MPI-M Earth System Model: ECHAM6, Journal of Advances in Modeling Earth Systems, 5, 146–172, https://doi.org/10.1002/jame.20015, 2013.

Swartzendruber, P., Chand, D., Jaffe, D., Smith, J., Reidmiller, D., Gratz, L., Keeler, J., Strode, S., Jaeglé, L., and Talbot, R.: Vertical distribution of mercury, CO, ozone, and aerosol scattering coefficient in the Pacific Northwest during the spring 2006 INTEX-B campaign, Journal of Geophysical Research: Atmospheres, 113, 2008.

Swartzendruber, P. C., Jaffe, D. A., Prestbo, E., Weiss-Penzias, P., Selin, N. E., Park, R., Jacob, D. J., Strode, S., and Jaegle, L.: Observations of reactive gaseous mercury in the free troposphere at the Mount Bachelor Observatory, Journal of Geophysical Research: Atmospheres, 111, 2006.

Swartzendruber, P.; Chand, D.; Jaffe, D. A.; Smith, J.; Reidmiller, D.; Gratz, L.; Keeler, J.; Strode, S.; Jaegle, L.; Talbot, R. Vertical distribution of mercury, CO, ozone, and aerosol scattering coefficient in the Pacific Northwest during the spring 2006 INTEX-B campaign. J. Geophys. Res., [Atmos.] 2008, 113, D10305.

Talbot, R., Mao, H., Scheuer, E., Dibb, J., and Avery, M.: Total depletion of Hg in the upper troposphere–lower stratosphere, Geophysical Research Letters, 34, 2007.

Talbot, R., Mao, H., Scheuer, E., Dibb, J., Avery, M., Browell, E., Sachse, G., Vay, S., Blake, D., Huey, G., and others: Factors influencing the large-scale distribution of Hg° in the Mexico City area and over the North Pacific, Atmospheric Chemistry and Physics, 8, 2103–2114, 2008.

Taylor, K. E., Williamson, D., and Zwiers, F.: The sea surface temperature and sea ice concentration boundary conditions for AMIP II simulations", PCMDI Report 60, Program for Climate Model Diagnosis and Intercomparison,Lawrence Livermore National Laboratory, 2000.

Thurnherr, I., Kozachek, A., Graf, P., Weng, Y., Bolshiyanov, D., Landwehr, S., Pfahl, S., Schmale, J., Sodemann, H., Steen-Larsen, H. C., and others: Meridional and vertical variations of the water vapour isotopic composition in the marine boundary layer over the Atlantic and Southern Ocean, Atmospheric Chemistry and Physics, 20, 5811–5835, 2020.

Tremoy, G., Vimeux, F., Cattani, O., Mayaki, S., Souley, I., and Favreau, G.: Measurements of water vapor isotope ratios with wavelength-scanned cavity ring-down spectroscopy technology: New insights and important caveats for deuterium excess measurements in tropical areas in comparison with isotope-ratio mass spectrometry, Rapid Communications in Mass Spectrometry, 25, 3469–3480, https://doi.org/10.1002/rcm.5252, 2011.

Tremoy, G., Vimeux, F., Mayaki, S., Souley, I., Cattani, O., Risi, C., Favreau, G., and Oi, M.: A 1-year long δ18O record of water vapor in Niamey (Niger) reveals insightful atmospheric processes at different timescales, Geophysical Research Letters, 39, 2012.

Tremoy, G., Vimeux, F., Soumana, S., Souley, I., Risi, C., Favreau, G., and Oï, M.: Clustering mesoscale convective systems with laser-based water vapor δ18O monitoring in Niamey (Niger), Journal of Geophysical Research: Atmospheres, 119, 5079–5103, https://doi.org/10.1002/2013JD020968, 2014.

1103   Wang, H., Fyke, J. G., Lenaerts, J. T. M., Nusbaumer, J. M., Singh, H., Noone, D., Rasch, P. J., and
1104   Zhang, R.: Influence of sea-ice anomalies on Antarctic precipitation using source attribution in the
1105   Community Earth System Model, The Cryosphere, 14, 429–444, https://doi.org/10.5194/tc-14-429-
1106   2020, 2020.

1107   Weiss-Penzias, P.; Gustin, M. S.; Lyman, S. N. Observations of speciated atmospheric mercury at three
1108   sites in Nevada: Evidence for a free tropospheric source of reactive gaseous mercury. J. Geophys. Res.
1109   [Atmos.] 2009, 114, D14302.

1110

1111   Weng, Y., Touzeau, A., and Sodemann, H.: Correcting the impact of the isotope composition on the
1112   mixing ratio dependency of water vapour isotope measurements with cavity ring-down spectrometers,
1113   Atmospheric Measurement Techniques, 13, 3167–3190, https://doi.org/10.5194/amt-13-3167-2020,
1114   2020.

1115   Worden, J., Noone, D., and Bowman, K.: Importance of rain evaporation and continental convection
1116   in the tropical water cycle., Nature, 445, 528–532, https://doi.org/10.1038/nature05508, 2007.

1117
1118